*powders*

MDPI

*Article*

# Multidimensional Particle Separation by Tilted-Angle Standing Surface Acoustic Waves—Physics, Control, and Design

**Sebastian Sachs *, Jörg König and Christian Cierpka**

Institute of Thermodynamics and Fluid Mechanics, Technische Universität Ilmenau, Am Helmholtzring 1, 98693 Ilmenau, Germany; joerg.koenig@tu-ilmenau.de (J.K.); christian.cierpka@tu-ilmenau.de (C.C.)
* Correspondence: sebastian.sachs@tu-ilmenau.de

**Abstract:** Lab-on-a-Chip devices based on tilted-angle standing surface acoustic waves (tasSAWs) emerged as a promising technology for multidimensional particle separation, highly selective in particle size and acoustic contrast factor. For this active separation method, a tailored acoustic field is used to focus and separate particles on stationary pressure nodes by means of the acoustic radiation force. However, additional non-linear acoustofluidic phenomena, such as the acoustically induced fluid flow or dielectrophoretic effects, are superimposed on the separation process. To obtain a particle separation of high quality, control parameters that can be adjusted during the separation process as well as design parameters are available. The latter are specified prior to the separation and span a high-dimensional parameter space, ranging from the acoustic wavelength to the dimensions and materials used for the microchannel. In this paper, the physical mechanisms to control and design tasSAW-based separation devices are reviewed. By combining experimental, semi-analytical, and numerical findings, a critical channel height and width are derived to suppress the influence of the acoustically induced fluid flow. Dealing with the three-dimensional nature of the separation process, particles are focused at different height levels of equal force balance by implementing a channel cover of high acoustic impedance while achieving an approx. three-times higher acoustic pressure. Using this improved channel design, the particle shape is identified as an additional separation criterion, rendering the continuous acoustofluidic particle separation as a multidimensional technology capable of selectively separating microparticles below 10 µm with regard to size, acoustic contrast, and shape.

**Keywords:** particle separation; surface acoustic waves; acoustofluidics; tilted-angle surface acoustic waves

check for updates

Academic Editors: Urs Alexander Peuker, Alfred P. Weber, Einar Kruis and Doris Segets

Received: 15 November 2024
Revised: 19 December 2024
Accepted: 3 January 2025
Published: 8 January 2025

**Citation:** Sachs, S.; König, J.; Cierpka, C. Multidimensional Particle Separation by Tilted-Angle Standing Surface Acoustic Waves—Physics, Control, and Design. *Powders* **2025**, *4*, 2. https://doi.org/10.3390/powders4010002

**Copyright:** © 2025 by the authors. Licensee MDPI, Basel, Switzerland. This article is an open access article distributed under the terms and conditions of the Creative Commons Attribution (CC BY) license (https://creativecommons.org/licenses/by/4.0/).

## 1. Introduction

Highly specific particle suspensions with a defined distribution in the material properties are key for high-quality products in process engineering, life science, biomedicine, and pharmacology [1–3]. To achieve the required composition in micro- and nanoparticle suspensions, numerous separation technologies based on miniaturized Lab-on-a-Chip devices emerged successfully [4–7]. These technologies led to the development of passive and active devices. Passive devices are robust and enable a high throughput by means of special channel geometries [8–10], embedded microstructures [11], or filtration systems [12,13]. In contrast, active devices are characterized by a higher flexibility and scalability, utilizing, for example, electric [14–16], magnetic [17–19], or acoustic fields [20,21]. In recent years, surface acoustic waves (SAWs) integrated in microfluidic devices have been demonstrated

as a label-free, biocompatible, and non-invasive technology for continuous particle separation [22–25]. In those devices, the trajectories of suspended particles are manipulated by tailored acoustic fields utilizing the acoustic radiation force and Stokes' drag due to the acoustically induced fluid flow [26,27]. Exploiting the scaling of the acoustic radiation force with the particle volume [28,29] and acoustic contrast factor [30–32], i.e., the density and isentropic compressibility of the particles relative to the surrounding fluid, particles can be separated in a multidimensional manner regarding their size, density, and compressibility.

Besides traveling SAWs, particle separation devices that superimpose standing SAWs (sSAWs) with stationary pressure nodes and antinodes on a pressure-driven main flow have emerged successfully [33–35]. This sSAW causes a three-dimensional pressure field inside the fluid domain. Due to the acoustic radiation force, particles with a positive or negative acoustic contrast factor are focused on the pressure nodes or antinodes in these devices, respectively. Based on this concept, devices with an sSAW aligned at a tilted angle relative to the side walls of an attached microchannel, so-called tilted-angle sSAW (tasSAW), were demonstrated to selectively separate several particle species across multiple pressure nodes [36]. Within these acoustofluidic devices, the motion of suspended particles is mainly determined by the interplay of the acoustic radiation force, which acts on particles with a positive acoustic contrast factor towards the nearest pressure node, and Stokes' drag due to the main flow. Particles whose motion is dominated by the acoustic radiation force will follow the tilted pressure nodes, which leads to a lateral displacement along the channel width. Conversely, particles dominated by the pressure-driven main flow follow their original path without lateral displacement. At the end of the acoustic manipulation, different particle species with sizes down to 100 nm can be extracted in separate outlets [37].

However, the particle behavior is further affected by multiphysical phenomena such as acoustophoresis, dielectrophoresis, drag, gravity, and buoyancy as depicted in Figure 1. In particular, the pattern of the acoustic fields, the electric field accompanying the sSAW due to the piezoelectric effect, and non-linear acoustofluidic phenomena, such as the acoustically induced fluid flow, largely determine the separation. These physical mechanisms are defined by a high-dimensional parameter space including control and design parameters; see Figure 1. The former comprise the volume flow rate and the supplied electrical power to adjust the fluid velocity and the amplitude of the tasSAW during the separation, respectively. Conversely, design parameters need to be specified prior to the particle separation and significantly affect the interplay of the multiphysical phenomena. Because of the high number of physical phenomena involved, depending not only on design and control parameters but also on boundary conditions such as material properties of the microfluidic device that are often not well known, experiments and simulations are required to gain profound understanding for the optimization of tasSAW-based devices.

In this study, the findings of project B13 (Grant Number 444806275) within the priority programme PP2045 "MehrDimPart" of the German Research Foundation are summarized in a systematic analysis of the influence of key design parameters on the acoustofluidic phenomena relevant to the particle separation. In Section 2, the working principle, control, and design parameters of tasSAW-based particle separation, as well as the experimental and numerical methods used, are described. Subsequently, particle trajectories are calculated using a simplified semi-analytical model in Section 3.1. Based on the model, the influence of different design parameters on the separation of a multimodal particle suspension is analyzed. Limitations of the simplified model are revealed, which require more sophisticated models and experiments incorporated subsequently. Among these, a combination of experimental findings and two-dimensional numerical simulations are utilized to evaluate the influence of the acoustically induced fluid flow in Section 3.2. As a result, important guidelines for the design of acoustofluidic separation devices are derived.

However, the particle separation is three-dimensional in nature, which is analyzed based on the positions of focused particles and the acoustically induced fluid flow at the outer regions of the sSAW in Section 3.3. To gain insight into the underlying acoustic fields and forces that dominate the experimentally observed particle behavior, a three-dimensional numerical model was set up. Based on the numerical model, particle trajectories are calculated that are in excellent agreement with the experiments and reveal benefits in using a channel cover of high acoustic impedance. Since the acoustic radiation force emerges from gradients in the acoustic fields, the particle shape is investigated as a further separation criterion in Section 3.4. The numerically calculated difference in the acoustic force on a prolate spheroid and a sphere of identical volume is revealed to be significant. Hence, the use of tasSAW-based devices renders the particle separation multidimensional in the separation criteria, including the particle size, shape, and acoustic contrast factor. Finally, the results are summarized in Section 4.

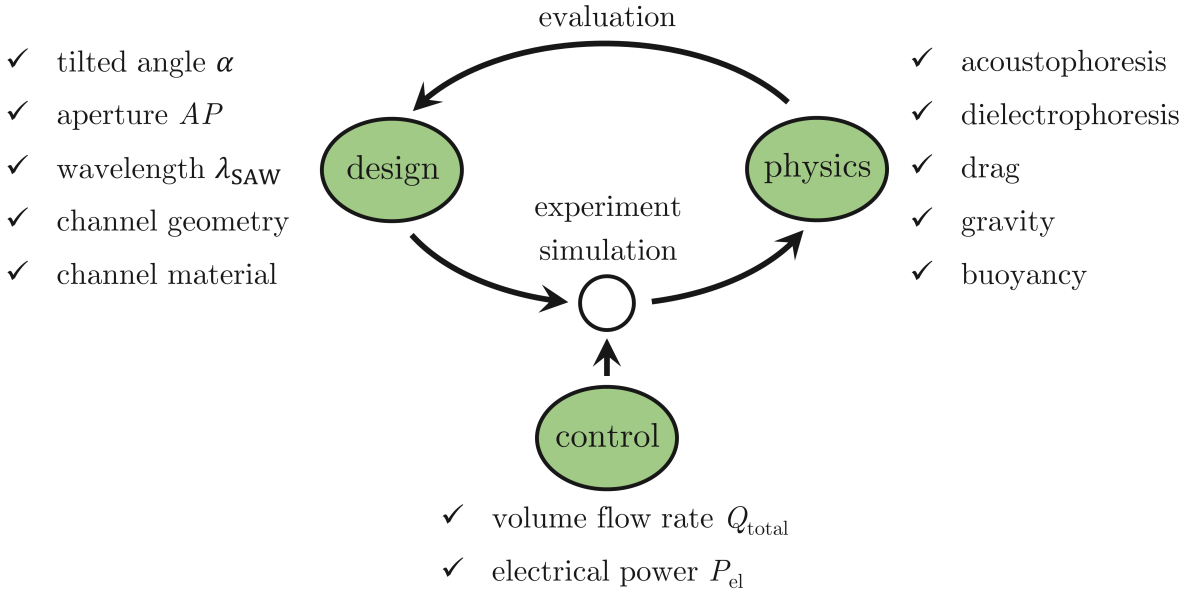


**Figure 1.** Schematic representation of the work flow applied in this project, where the multiphysical phenomena were studied by experiments and numerical simulations in conjunction with crucial design and control parameters. Based on the correlations found between the particle behavior and the parameters set, the design of the acoustofluidic device was revised systematically.

## 2. Methods

### *2.1. Particle Separation Using tasSAW Devices*

In Figure 2, an acoustofluidic device to separate microparticles based on tasSAWs is depicted schematically. The device consists of a pair of interdigital transducers (IDTs) with periodically arranged finger electrodes of width and spacing $w = \lambda_{SAW}/4$, which are deposited on a 128° rotated Y-cut of lithium niobate ($LiNbO_3$). Here, the wavelength of the SAW is indicated by $\lambda_{SAW}$. Applying an alternating voltage of frequency $f = c_s/\lambda_{SAW}$ to the IDTs causes elastic surface deformations that superimpose in the region of the IDTs [38]. Here, $c_s$ denotes the resulting phase velocity of the SAW along the crystallographic X-direction of the substrate. With the bidirectional IDT, the SAWs propagate to both sides. While the waves traveling outwards are fully damped by a layer of photoresist, the counter-propagating SAWs are superimposed between the two IDTs to form an sSAW. A straight microchannel made of polydimethylsiloxane (PDMS, Sylgard 184, Dow Corning) with a rectangular cross-section (width $W$ and height $H$) is placed at a tilt angle $\alpha$ relative to the IDTs on top of the $LiNbO_3$ substrate. As soon as the SAWs reach the microchannel, energy is radiated into the channel side walls and the fluid inside the channel, causing the SAWs to

be attenuated. The radiated energy drives longitudinal bulk acoustic waves (BAWs) with a wavelength of $\lambda_{BAW} = c_0/c_s\lambda_{SAW}$ within the fluid domain [39]. Here, the speed of sound in the fluid is indicated by $c_0$. Due to deviating acoustic impedances of the fluid $Z_{fluid}$ and PDMS $Z_{PDMS}$, the BAWs are partially reflected at the channel side walls and ceiling as given by the reflection coefficient $R_1 = (Z_{PDMS} - Z_{fluid})/(Z_{PDMS} + Z_{fluid})$. By superimposing the propagating and reflected BAWs, a pseudo-standing acoustic wave field with stationary pressure nodes and antinodes aligned at the same angle $\alpha$ relative to the channel side walls is generated in the fluid. Besides standing wave components, the acoustic wave field is further characterized by travelling wave components [40]. These arise both along the channel width and height due to the attenuation of the SAWs and the partial reflection and attenuation of the BAWs, respectively. Furthermore, a laminar fluid flow is induced acoustically in the confined microchannel due to the attenuation of the BAWs in the fluid via the so-called acoustic streaming effect [41].

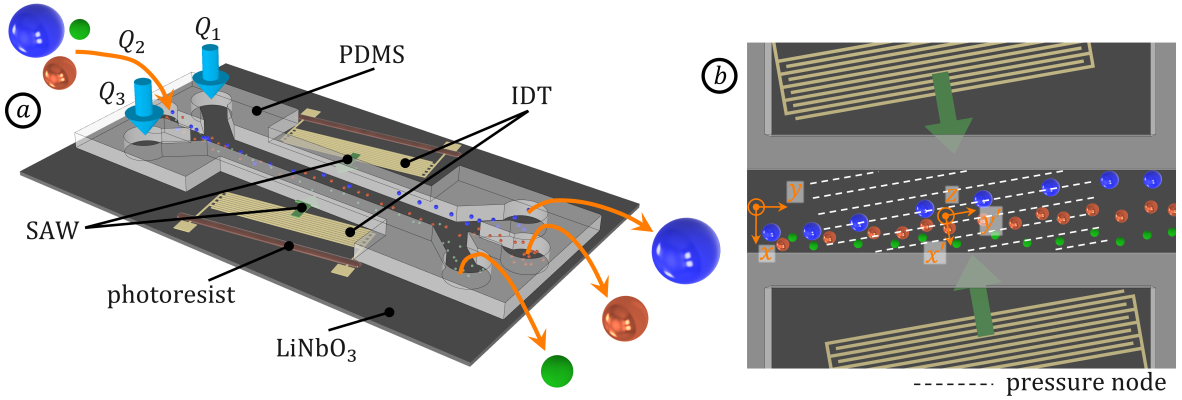


**Figure 2.** Schematic of the acoustofluidic device using tasSAW to separate three particle species from a mixture (**a**), which is inserted with the volume flow rate $Q_2$. For visualization purposes, the PDMS cover to seal the microchannel was omitted. Top view of the particle separation with pressure nodes indicated by dashed lines and the rotated coordinate system $(x', y', z)$ (**b**).

By using a syringe pump, pure fluid and a particle mixture are supplied to the outer and central inlets, respectively. The suspended particles are pre-positioned in a narrow band close to one channel side wall by adjusting the volume flow rates $(Q_1, Q_2, Q_3)$. Within the acoustic field, the acoustic radiation force $\boldsymbol{F}_{rad}$ applied on spherical particles with radius $r \ll \lambda_{SAW}$ is defined by gradients in the acoustic pressure $p_1$ and velocity field $\boldsymbol{u}_1$ as [42]

$$\boldsymbol{F}_{rad} = -\pi r^3 \left[ \frac{2\kappa_0}{3} Re(f_1^* p_1^* \boldsymbol{\nabla} p_1) - \rho_0 Re(f_2^* \boldsymbol{u}_1^* \cdot \boldsymbol{\nabla} \boldsymbol{u}_1) \right], \tag{1}$$

$$f_1 = 1 - \frac{\kappa_p}{\kappa_0}, \tag{2}$$

$$f_2 = \frac{2\left(1 + \frac{3\delta}{2r}\left[1 + i\left(1 + \frac{\delta}{r}\right)\right]\right)(\rho_p - \rho_0)}{2\rho_p + \rho_0\left(1 + \frac{9\delta}{2r}\left[1 + i\left(1 + \frac{\delta}{r}\right)\right]\right)}. \tag{3}$$

Here, the asterisk indicates complex conjugation, and $Re(X)$ is the real part of a quantity $X$. The density and isentropic compressibility of the undisturbed fluid are denoted by $\rho_0$ and $\kappa_0$, respectively, and those of the particles by $\rho_p$ and $\kappa_p$, respectively. The monopole and dipole scattering coefficients $f_1$ and $f_2$ are calculated using the frequency-dependent viscous boundary layer thickness $\delta = \sqrt{\mu_0/\pi f \rho_0}$, where $\mu_0$ is the shear viscosity of the undisturbed fluid. According to Equation (1), the magnitude of $\boldsymbol{F}_{rad}$ depends on the particle volume and material, which is quantified by the acoustic contrast factor $\phi(\rho_p, \kappa_p) = 1/3 f_1 + 1/2 Re(f_2)$ [42]. Both quantities serve as separation criteria and define the multidimensional particle descriptor vector. In addition, the Stokes' drag

$\boldsymbol{F}_{\text{drag}} = 6\pi\mu_0 r\boldsymbol{u}_{\text{r}}$ acts on the particles due to a relative velocity $\boldsymbol{u}_{\text{r}}$ between the particles and the fluid flow, induced either from the acoustic streaming effect or the main flow imposed by the total volume flow rate. By applying Newton's second law and neglecting particle–particle interactions, dielectrophoretic forces, acoustothermal effects, and thermally driven flows [43–46], an influence of the particles on the flow and wall effects [47], the trajectories of spherical particles are determined by

$$\frac{4}{3}\pi r^3\rho_{\text{p}}\frac{d\boldsymbol{u}_{\text{p}}}{dt} = \boldsymbol{F}_{\text{rad}} + \boldsymbol{F}_{\text{drag}} + \frac{4}{3}\pi(\rho_{\text{p}} - \rho_0)r^3\boldsymbol{g}, \tag{4}$$

where $\boldsymbol{u}_{\text{p}}$ is the particle velocity and $\boldsymbol{g}$ the acceleration due to gravity. Depending on the particle descriptor vector, the motion of microparticles is either dominated by $\boldsymbol{F}_{\text{rad}}$ or $\boldsymbol{F}_{\text{drag}}$ due to the fluid flow. While for the latter case, particles remain on their original paths, particles dominated by $\boldsymbol{F}_{\text{rad}}$ follow the tilted pressure nodes and are shifted in the $x$-direction along the channel width. In this way, particles can be separated according to their size and material and collected in different outlets at the end of the microchannel.

The acoustofluidic device is characterized by control and design parameters as depicted in Figure 1. Control parameters include the total volume flow rate $Q_{\text{total}} = Q_1 + Q_2 + Q_3$ and the electrical power $P_{\text{el}}$ transmitted to the IDTs, which can be adjusted during the separation process and establish a high flexibility of the system. Furthermore, the pre-positioning of the particles is affected by the ratio between the individual volume flow rates $Q_1$, $Q_2$, and $Q_3$, which can be adjusted during the separation process. The influence of the pre-positioning is discussed by Peng et al. (2022) [48] in detail. In contrast, design parameters need to be specified prior to the separation. These define a high-dimensional parameter space including the channel geometry, the channel material, the wavelength of the SAW $\lambda_{\text{SAW}}$, the tilt angle $\alpha$, the aperture $AP$ of the IDTs, and the distance $L$ between the IDTs. To optimize the separation process, both the design and control parameters have to be considered. In this study, the influence of these parameters on the particle separation is analyzed by various experimental investigations and numerical simulations in different degrees of abstraction.

### *2.2. Experimental Investigation*

To investigate the influence of the control and design parameters on the particle separation, the behavior of fluorescence-labeled polystyrene particles suspended in deionized water or aqueous glycerol was examined experimentally. For this, the acoustofluidic device (see Figure 2) was mounted on top of an inverted microscope equipped with a Plan-Neofluar objective (M20×, NA = 0.4, Zeiss GmbH, Oberkochen, Germany). The particle suspension (PS-FluoRed, MicroParticles GmbH, Berlin, Germany) was pumped through a microchannel made of PDMS with a rectangular cross-section of width $W$ and height $H$ without pulsation using a syringe pump (neMESYS, cetoni GmbH, Korbussen, Germany). The microchannel features air pockets to limit the thickness of the channel side walls in the region of the IDTs to 500 µm. As the SAWs pass the substrate-PDMS interface, part of their energy is radiated into the channel side walls, which leads to a significant attenuation of the SAWs. In particular, Kiebert et al. (2017) [49] measured a loss of up to 96 % of the acoustic energy carried by an SAW with a wavelength of 30 µm due to a 500 µm thick PDMS wall. The acoustic waves propagating in the PDMS domain are strongly damped and totally reflected at the PDMS-fluid interface due to the small angle of incidence [49]. Since these waves are not coupled directly from the PDMS in the fluid, they were neglected in the further modeling. A PowerSAW generator (BelektroniG GmbH, Freital, Germany) was used to excite the SAWs with an adjustable electrical power $P_{\text{el}}$ at a constant frequency $f$.

Details on the optical setup, fabrication of the acoustofluidic device, and experimental procedure can be found in our previous works [50,51].

The three-dimensional positions $(x, y, z)$ of spherical particles within the fluid domain were measured using astigmatism particle tracking velocimetry (APTV, [52]). This optical measurement technique relies on elliptical distortions of the particle images caused by a cylindrical lens installed in front of the camera. Based on a calibration function, the lengths of the semi-axes $(a_x, a_y)$ of the elliptical particle images are mapped to the depth position $(z)$ of the particles [53]. With the positions at hand, the individual particles were tracked in consecutive frames by applying a simple nearest neighbor tracking algorithm to determine the corresponding displacement vectors $\boldsymbol{d}$. With the well-known time interval $\Delta t$ between the frames, the particle velocity $\boldsymbol{u}_\mathrm{p}$ can be inferred. Assuming the particles faithfully follow the fluid flow, velocity fields were reconstructed from an ensemble of individual particle vectors in a Lagrangian and Eulerian framework. For details on the image processing, sub-pixel accurate determination of the in-plane positions $(x, y)$, measurement procedure, and reconstruction of the velocity fields, the interested reader is referred to our previous works [50,51,54–56].

Due to the correlation between the depth position and the particle image shape $z = f(a_x, a_y)$ through a calibration function, monodisperse particles are typically used in APTV measurements. However, particles with multimodal size distribution are inherently employed in particle separation experiments. For this purpose, the APTV was extended in our previous work to include a particle size recognition based on the particle images [55]. The developed algorithm utilizes either a deterministic approach based on the particle image intensity or a deep neural network. In a comprehensive study, the algorithm classified dense particle suspensions with multimodal size distribution with a precision of up to 99.3 %. Based on the classification, individual calibration functions can be applied to the different particle sizes to derive the depth position of the particles precisely. A detailed description and uncertainty analysis of the size recognition algorithm can be found in Sachs et al. (2023) [55].

Besides spherical particles, the kinematic behavior of prolate spheroids was investigated by optical microscopy using an inverted fluorescence microscope. Based on a developed detection algorithm, the in-plane $(\varphi)$ and out-of-plane $(\theta)$ orientations as well as the in-plane positions $(x, y)$ of the non-spherical particles were determined [57]. To analyze the particle distribution along the channel height without measuring the $z$-position of the particles, the measurement volume was traversed in fine steps in the $z$-direction. By applying rigorous outlier filters for defocused particle images, the three-dimensional particle distribution was derived based on the number of valid detections in the different measurement volumes. Details of the underlying algorithm and an uncertainty analysis can be found in our previous studies [57,58].

### *2.3. Numerical Simulation*

To reveal the physical mechanisms underlying the experimental findings, two- and three-dimensional numerical models were set up. The numerical results provide insights into the acoustic fields and forces acting on the suspended particles, which are key to analyzing the influence of design parameters on the particle separation and cannot directly be measured. Based on the perturbation theory, a field quantity $g$ is expanded up to the second order using the smallness parameter $\epsilon$ according to [59]

$$g = g_0 + \epsilon g_1 + \epsilon^2 g_2. \tag{5}$$

While stationary background fields are described in zeroth-order quantities, time-harmonic acoustic fields and non-linear acoustic phenomena are captured as first-order

and second-order quantities, respectively. The difference in the typical time scales of the first- and second-order phenomena allows an initial calculation of the acoustic fields in the frequency domain. The acoustic quantities are subsequently used as source terms to calculate the second-order quantities, such as the induced fluid flow. The full set of thermoviscous partial differential equations [60–62] governing the acoustic phenomena was solved numerically in a two-dimensional numerical model, which covered the channel cross-section of the fluid domain. To calculate the first-order field quantities, the "Thermoviscous Acoustics" interface in the commercial software Comsol Multiphysics® 5.6 [63] was used. The mesh was greatly refined towards the boundaries of the fluid–PDMS interfaces to correctly resolve the thin thermoviscous boundary layers. A schematic representation of the meshed computational domain with applied boundary conditions is given in Figure A1 (Appendix A). At the channel bottom, the surface-normal displacement of the sSAW was prescribed analytically as a boundary condition. Following the approach in our previous work [51], a slip condition was implemented on the longitudinal surface displacement by the sSAW, which yielded excellent agreement with the experimentally determined fluid flow. Impedance boundary conditions were set at the fluid–PDMS interfaces to model the partial reflection of the acoustic waves without the need to model the channel side walls and ceiling explicitly. Based on the numerically derived first-order quantities, i.e., the first-order velocity $\boldsymbol{u}_1$, pressure $p_1$, and density $\rho_1$, the second-order fluid velocity $\boldsymbol{u}_2$ and pressure $p_2$ were calculated with a stationary solver using the "Laminar Flow" interface in Comsol Multiphysics® 5.6 [63]. Finally, the measured velocity fields were used to validate the numerical model (see Section 3.2). Far more details on the numerical model, implemented boundary conditions, material parameters, a mesh independence study, and the adaptation of critical model parameters can be found in Sachs et al. (2022) [51].

Experiments on the particle separation in acoustofluidic devices revealed significant three-dimensional effects [54], which were analyzed in extended numerical models. To limit the numerical effort, the thin thermoviscous boundary layers were not resolved in the three-dimensional model. In this way, the acoustic pressure field was calculated based on a Helmholtz equation, where viscous and thermal losses in the fluid bulk were captured by damping coefficients [64,65]. To solve for the first-order fields, the "Pressure Acoustics" interface was used in the frequency domain according to our previous work [57]. This enabled the calculation of the 3D acoustofluidic phenomena at the high-performance computing cluster of TU Ilmenau using AMD EPYC 7601 (2.2 GHz) processors with up to 2 TB of random-access memory. As depicted schematically in Figure A2a (Appendix A), the numerical model covered half of the channel cross-section and 1.6 mm in the $y$-direction, while symmetry conditions were set in the $yz$-plane at $x = 0$ and in the $xz$-plane at $y = AP/2$. To calculate the second-order quantities, a "Laminar Flow" interface was again used similarly to the two-dimensional model. All calculations based on the three-dimensional model were carried out in Comsol Multiphysics® 6.1. By neglecting the particle inertia, trajectories of spherical particles were determined based on Equation (4) with bounce-back boundary conditions at all margins of the fluid domain. However, to determine the resulting forces on a prolate spheroid, the non-spherical particle was modeled as a solid within the fluid domain as shown in Figure A2b. At the fluid–solid interface, i.e., at the surface of the particle, an "Acoustic-Structure Boundary" [63] was set to ensure continuity. Although only prolate spheroids were used in this study, non-spherical particles of arbitrary shape with dimensions larger than the viscous boundary layer ($l \gg \delta$) can be simulated in the numerical model. The acoustic drag and radiation force acting on the particle were merged into the time-averaged acoustic force $\boldsymbol{F}$. To determine $\boldsymbol{F}$, the time-averaged second-order stress tensor $\langle \sigma_2 \rangle$ and momentum flux tensor $\rho_0 \langle \boldsymbol{u}_1 \boldsymbol{u}_1 \rangle$ were integrated across the particle equilibrium surface $S_0$ according to [66–68]

$$\boldsymbol{F} = \int_{S_0} \left[ \langle \boldsymbol{\sigma}_2 \rangle - \rho_0 \langle \boldsymbol{u}_1 \boldsymbol{u}_1 \rangle \right] \cdot \boldsymbol{n} \, dS, \tag{6}$$

where the outward-pointing normal vector at $S_0$ is indicated by $\boldsymbol{n}$. For a detailed description of the applied boundary conditions, material parameters, and fundamental equations, as well as a mesh independence study, the interested reader is referred to our previous works [57,58].

## 3. Results and Discussion

### *3.1. Acoustophoresis in tasSAW Devices*

The specific particle separation using tasSAWs is characterized by design and control parameters that define a high-dimensional parameter space (see Section 2.1). To reveal underlying dependencies of the separation on critical design parameters, a semi-analytical model [36] is adapted based on an analytical expression for the acoustic pressure $p_1$ in the rotated coordinate system $(x', y', z)$ (see Figure 2b) according to

$$p_1 = \frac{p_\mathrm{a}}{\hat{\zeta}} \zeta(x', y', z) i e^{i\omega t}, \tag{7}$$

$$\zeta(x', y', z) = \left[ e^{ikx' + C_\mathrm{d}(x' - W/(2\cos\alpha) + y'\tan\alpha)} - e^{-i(kx'+\pi) - C_\mathrm{d}(x' + W/(2\cos\alpha) + y'\tan\alpha)} \right] \cdot \left[ e^{-(ik_z + C_\mathrm{f})z} + R_1 e^{ik_z z + C_\mathrm{f}(z-2H)} \right], \tag{8}$$

$$p_\mathrm{a} = \frac{\hat{A}(2\pi f)^2 \rho_0}{ik_z + C_\mathrm{f}}. \tag{9}$$

The normalized pattern of $p_1$ is given by $\zeta/\hat{\zeta}$, which takes into account the superposition of counter-propagating SAWs as well as the reflection of BAWs at the channel ceiling. Using the speed of sound in the fluid $c_0$, the attenuation of SAWs and BAWs is considered by attenuation coefficients $C_\mathrm{d} = \rho_0 c_0 / (\rho_\mathrm{s} c_\mathrm{s} \lambda_\mathrm{SAW})$ [69] and $C_\mathrm{f} = b(2\pi f)^2/(2\rho_0 c_0)$ [70], respectively. Here, $\rho_\mathrm{s}$ denotes the density of $LiNbO_3$, and $b = 4/3\mu_0 + \mu_0'$ is a function of the bulk viscosity $\mu_0'$. The wave numbers of the SAW and BAW are indicated by $k = 2\pi/\lambda_\mathrm{SAW}$ and $k_z = 2\pi c_\mathrm{s}/(c_0 \lambda_\mathrm{SAW})$, respectively. The pressure amplitude $p_\mathrm{a}$ is scaled by the surface-normal displacement amplitude of the SAW $\hat{A} = \sqrt{k_\eta P_\mathrm{el} \lambda_\mathrm{SAW}/(F_\mathrm{N}\, AP)}$ [71]. Here, the coupling factor $k_\eta$ [51] and the material-dependent factor $F_\mathrm{N} = 2.47 \times 10^{15}\ \mathrm{W/m^2}$ are used [71]. To determine the acoustic velocity field $\boldsymbol{u}_1$, its surface normal component $u_{1,z}$ is phase-shifted by $\pi/2$ via multiplication with the imaginary unit $i$ and a sign change according to

$$\boldsymbol{u}_1 = \frac{1}{2\pi f \rho_0} (\boldsymbol{e}_{x'} + \boldsymbol{e}_{y'} - i\boldsymbol{e}_z) \odot \boldsymbol{\nabla} p_1, \tag{10}$$

where the unity vectors are denoted by $(\boldsymbol{e}_{x'}, \boldsymbol{e}_{y'}, \boldsymbol{e}_z)$ and the Hadamard product by $\odot$. By combining Equations (1), (7), and (10), $\boldsymbol{F}_\mathrm{rad}$ is calculated analytically for various particle sizes and materials. Furthermore, Stokes' drag based on the velocity profile $\boldsymbol{u}_\mathrm{f}$ of a channel flow is superimposed with no-slip conditions at the channel boundaries [72]. Neglecting particle inertia and gravity, the planar particle velocity $\boldsymbol{u}_\mathrm{p} = (u_{\mathrm{p,x}}, u_{\mathrm{p,y}})^T$ is determined based on Equation (4) by

$$\boldsymbol{u}_\mathrm{p} = \begin{pmatrix} F_{\mathrm{rad},x'} \cos\alpha / (6\pi\mu_0 r) \\ u_{\mathrm{f,y}} - F_{\mathrm{rad},x'} \sin\alpha / (6\pi\mu_0 r) \end{pmatrix}. \tag{11}$$

The aim of this model is to gain insight into the physical dependencies of the separation process on critical design parameters at a reasonable numerical cost. Therefore, the particle trajectories are calculated only in the $xy$-plane at $z = H/2$ to allow for a broad variation of the design parameters. The model was validated using experimental data for the separation of particles with radii of 0.57 µm and 4.94 µm. In Figure 3a,b, measured particle positions are shown as markers at the beginning and end of the IDTs, respectively. In the experimental setup, the tilted angle amounted to approx. 5.8° to obtain a separation with high purity. The larger 4.94 µm polystyrene particles follow the tilted pressure nodes and are displaced in the positive $x$-direction after the acoustic manipulation. In contrast, the distribution of the 0.57 µm particles across the channel width widens significantly due to the influence of the acoustically induced fluid flow (see Figure 3b). The trajectories of both particle species calculated by the semi-analytical model are represented by path lines. Excellent agreement is found between the measured positions and calculated trajectories of the 4.94 µm particles. However, the broadening of the distribution of the 0.57 µm particles is not captured by the numerical model. This underlines the limitations of the model, in which the acoustically induced flow is not considered.

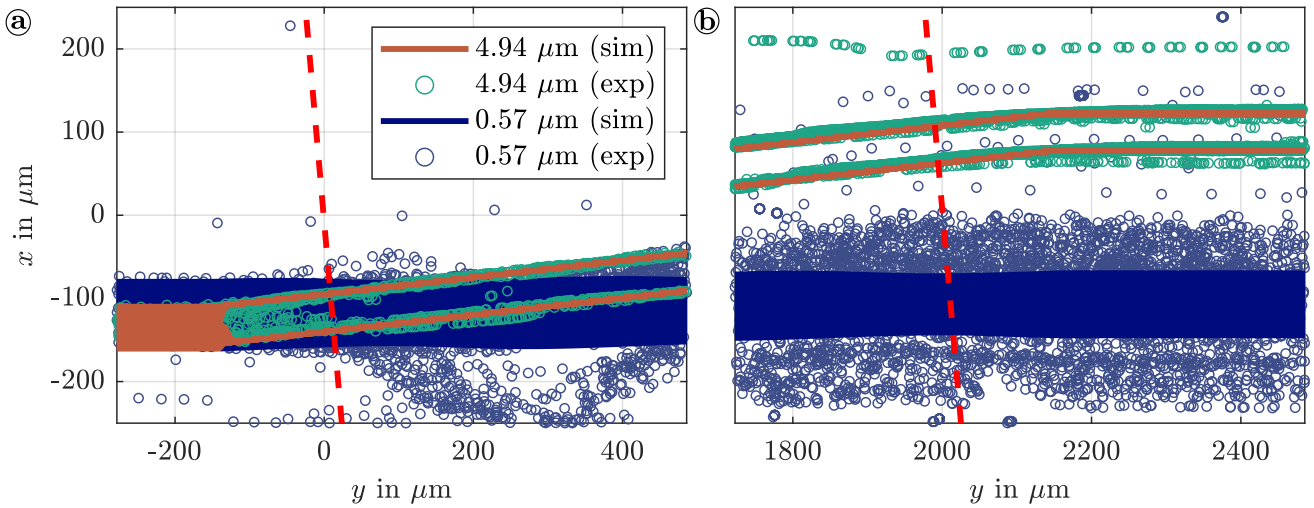


**Figure 3.** Measured positions (exp) and numerically calculated trajectories (sim) of polystyrene particles with two different sizes at the beginning (**a**) and end (**b**) of the IDTs. The edges of the opposite IDTs are indicated by red dashed lines.

Using the validated model, particle trajectories are calculated for three particle species of different radii and materials, as shown in Figures 4a and 4b, respectively. In the simulation, the particles were pre-positioned in a narrow band of 50 µm close to one channel side wall of a microchannel with a cross-section of 500 × 100 µm$^2$. The edges of the tasSAW are highlighted by dashed lines. In the model, the tilt angle was set to 11°, which allowed particles to almost reach the opposite channel side wall at the end of the acoustofluidic manipulation. In both cases, the particles with the largest radius or acoustic contrast factor follow the stationary pressure nodes, while particles with the smallest radius or acoustic contrast factor rather follow the main flow. At the end of the computational domain, the particle species are separated by $\Delta x_1$ or $\Delta x_2$ and can be collected in different outlets.

The scaling of $\boldsymbol{F}_{\mathrm{rad}}$ with the particle volume and the acoustic contrast factor further permits a multidimensional particle separation as shown in Figure 5. Instead of selecting discrete compositions in the separation criteria, particles with Gaussian distributions around radii of 1 µm and 2.5 µm and acoustic contrast factors around 0.16 and 0.5 were chosen as feed material, as commonly used in process engineering as well as biomedical and pharmaceutical applications, e.g., using particles made of silicon dioxide or polystyrene.

The standard deviation in both distributions amounts to 1 µm and 0.1 for the radii and acoustic contrast factors, respectively. The separation result is evaluated using the Tromp function $T$, which gives a measure for the probability of particles being separated into the concentrate [73–75]. According to Figure 5b, large particles with a high acoustic contrast factor ($T \ll 1$) and small particles with a low acoustic contrast factor ($T \approx 1$) are reliably separated. However, particles separated inconsistently are indicated in a narrow band, in which the Tromp function rises rapidly from $T \ll 1$ to $T \approx 1$. This narrow transition range is clearly visible based on the Shannon entropy $H$ [73–75] in Figure 5c. More than 85 % of the particles are located in a region of low entropy, $H < 0.05$, where the particles are consistently collected in the same outlet. However, the natural limits of the separation technique are reflected by a higher entropy, indicating particles that were pushed ambiguously into different outlets. This narrow band of higher entropy remains tilted in the $r\phi$-plane, highlighting the multidimensional separation effect by size and acoustic contrast factor.

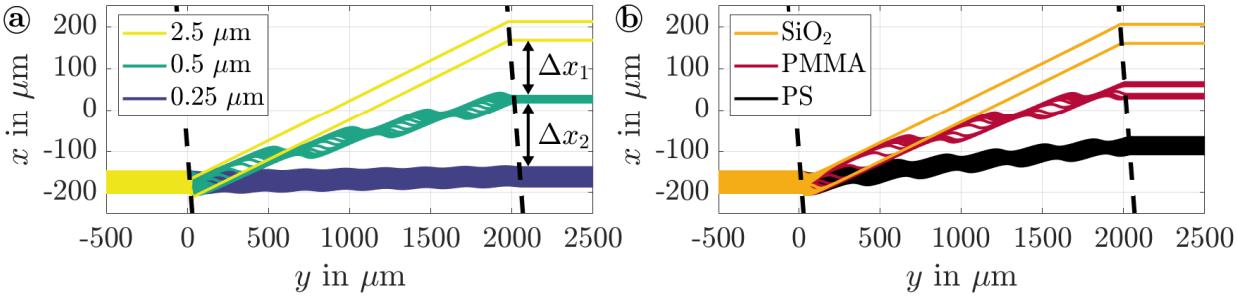


**Figure 4.** Numerically calculated trajectories of particles with (**a**) different radii ($Q_{\text{total}} = 1.67\,\mu\text{L}\,\text{min}^{-1}$, $P_{\text{el}} = 612.25\,\text{mW}$, polystyrene) and (**b**) materials ($Q_{\text{total}} = 5.04\,\mu\text{L}\,\text{min}^{-1}$, $P_{\text{el}} = 205.10\,\text{mW}$, $r = 1.25\,\mu\text{m}$, silicon dioxide ($SiO_2$), polymethylmethacrylate (PMMA), polystyrene (PS)). The motion of the particles is affected by a tasSAW with a tilt angle of $\alpha = 11°$ within the dashed lines. Main flow is applied in the positive $y$-direction.

To optimize design parameters, the separation result of three particle species with discrete descriptor vectors is quantified by the separation distance $\Delta x_{\text{sep}} = \Delta x_1 + \Delta x_2 - |\Delta x_1 - \Delta x_2|$. Here, $\Delta x_1$ and $\Delta x_2$ denote the minimum distances between the trajectories of different particle species. As exemplified in Figure 4a, $\Delta x_1$ and $\Delta x_2$ possess positive values if the respective particle species are spatially separated. However, if the trajectories of the different species overlap, $\Delta x_1$ or $\Delta x_2$ turns negative and gives a measure for the overlapping distance in the $x$-direction. In this case, a clear separation is impossible even with optimally positioned outlets, and $\Delta x_{\text{sep}}$ takes negative values. Conversely, a pure separation is feasible with optimally positioned outlets as long as $\Delta x_{\text{sep}}$ is positive. Trajectories of the different particle species are separated further, the larger $\Delta x_{\text{sep}}$. In turn, this provides more flexibility in the positioning of the outlets.

Based on the semi-analytical model, the separation of particles with radii of 0.25 µm, 0.5 µm, and 2.5 µm is studied by varying the tilt angle $\alpha$. Concurrently, the channel cross-section ($500 \times 100\,\mu\text{m}^2$), the wavelength ($\lambda_{\text{SAW}} = 90\,\mu\text{m}$), and the aperture ($AP = 2\,\text{mm}$) remain constant, while the control parameters ($Q_{\text{total}} = Q_1 + Q_2 + Q_3, P_{\text{el}}$) are treated as variables. A detailed discussion on the influence of the aperture of the IDTs is given below. Under experimental conditions, particles can adhere to the channel side walls made of PDMS, limiting the particle yield and long-term usability of the acoustofluidic device. Hence, to reduce the probability of adhering particles, a maximum tilt angle of $\alpha_{\text{max}} = \arctan\left((W/2 - \hat{x}_0)/AP\right)$ is set to ensure that particles can reach the opposite channel side wall at the end of the aperture at the earliest. The position of feed particles closest to the opposite channel side wall is indicated by $\hat{x}_0$.

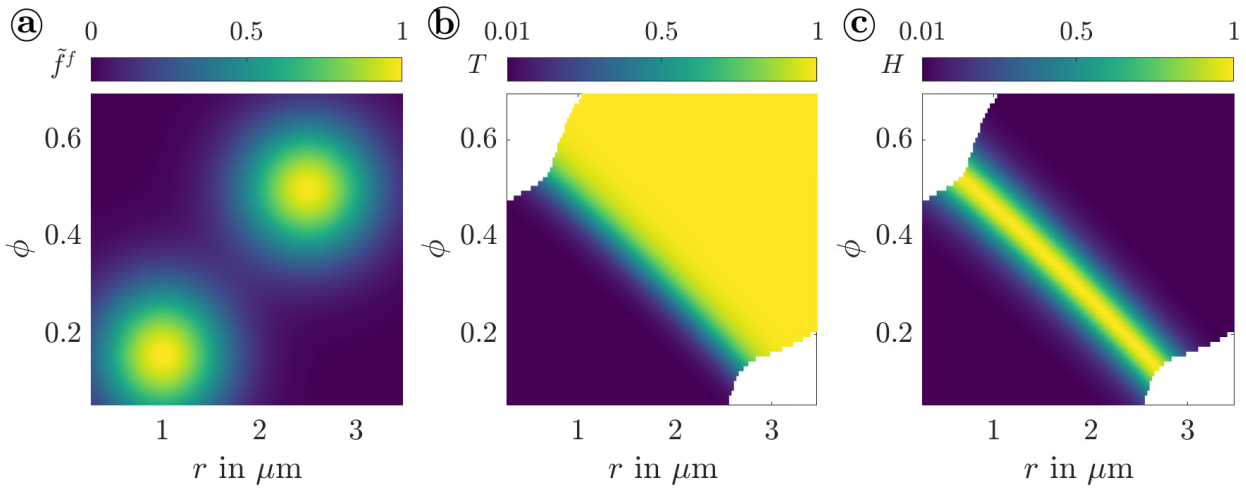


**Figure 5.** Multidimensional separation of feed particles with bimodal Gaussian-distributed radii and acoustic contrast factors as illustrated by the normalized probability density $\tilde{f}^f$ (**a**). The separation result with $Q_{\text{total}} = 4.18\,\mu\text{L}\,\text{min}^{-1}$, $P_{\text{el}} = 88.78\,\text{mW}$, and $\alpha = 11.3°$ is evaluated by a bivariate Tromp (**b**) and Shannon entropy function (**c**).

In Figure 6a,b, the maximum separation distance $\Delta\tilde{x}_{\text{sep}}$ (normalized by its maximum) and the corresponding angle $\alpha$ are illustrated against the control parameters, respectively. Three regions (I–III) are evident in the separation results. In regions I and III, a separation with less than half the separation distance ($\Delta\tilde{x}_{\text{sep}} < 0.5$) achievable with optimal settings of the control parameters is indicated, as the electrical power supplied to the IDTs is too low or too high for the given volume flow rate, respectively. As a result, the separation of the medium-sized 0.5 µm particles becomes challenging. However, a particle separation with $\Delta\tilde{x}_{\text{sep}} \geq 0.5$ is achieved in region II. Within this region of control parameters, the optimum tilt angle increases with $P_{\text{el}}$ for a given volume flow rate. Simultaneously, $\Delta\tilde{x}_{\text{sep}}$ increases up to a maximum along the red dashed line with a corresponding angle close to $\alpha_{\text{max}}$. In order to obtain widely separated particle trajectories in the given configuration, the tilt angle is thus set to $\alpha_{\text{max}}$ in further considerations. However, a smaller tilt angle revealed beneficial for particle separation with a higher throughput at a given input power $P_{\text{el}}$ as depicted in Figure 6b. Hence, to maximize the processable throughput at a limited input power, a smaller tilt angle is preferred. Please note that the evaluation was based on the separation of particles with radii of 0.25 µm, 0.5 µm, and 2.5 µm, and the optimal tilt angle might deviate for particle suspensions of different sizes [48,76].

The aperture of the IDTs affects the separation process in multiple ways. First, the acoustic radiation force scales $|\boldsymbol{F}_{\text{rad}}| \propto p_{\text{a}}^2 \propto 1/AP$ at a constant power $P_{\text{el}}$, which reduces the required electrical power to manipulate particle trajectories at a given volume flow rate as $AP$ decreases. Second, the maximum angle $\alpha_{\text{max}}$ increases with decreasing $AP$, causing the particle velocity parallel and perpendicular to the main flow direction to be reduced according to Equation (11). Third, the distance over which a particle can be manipulated also decreases with $AP$. Under the influence of these opposing effects, $AP$ is found to have a negligible effect on the separation result, as can be seen from the marginal variation of $\Delta\tilde{x}_{\text{sep}}$ in Figure 7. However, depending on the aperture, diffraction effects of the SAW emerge, which lead to local gradients in the amplitude of $\boldsymbol{F}_{\text{rad}}$ and acoustically induced fluid flows in the $y$-direction [77,78]. These effects are not included in the proposed model and are discussed in Section 3.3. For further investigations, the aperture was set constant at 2 mm.

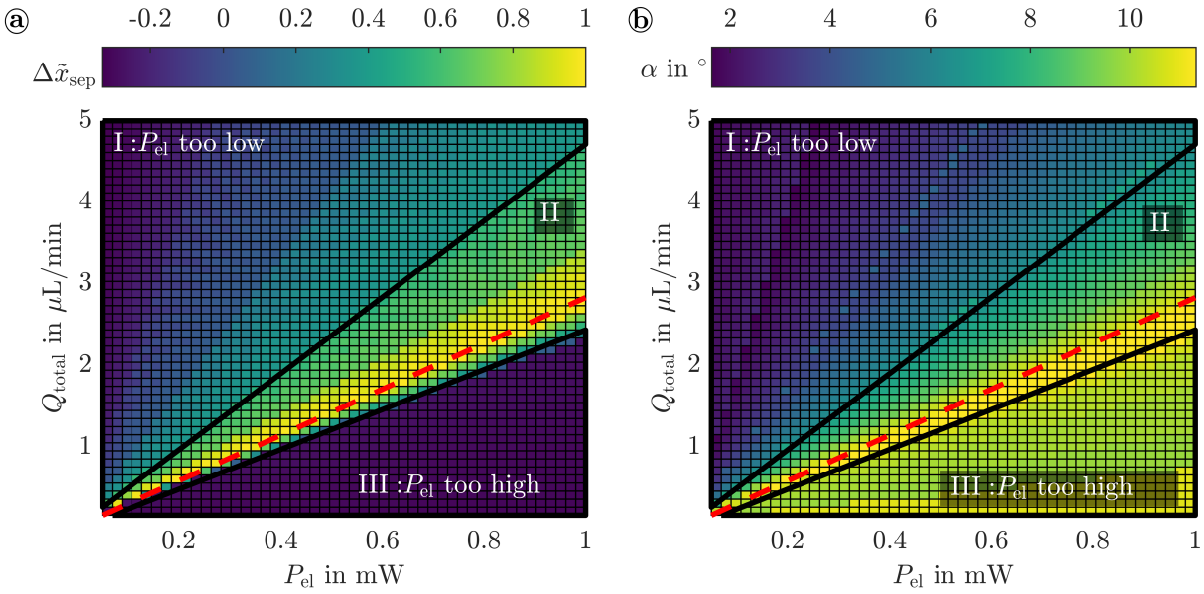


**Figure 6.** Evaluation of the separation of particles with radii of 0.25 µm, 0.5 µm, and 2.5 µm across the control parameters based on the normalized maximum separation distance $\Delta\tilde{x}_{sep}$ (**a**) and the respective tilt angle $\alpha$ (**b**). In regions I and III, a separation distance of $\Delta\tilde{x}_{sep} < 0.5$ is indicated, while results with $\Delta\tilde{x}_{sep} \geq 0.5$ are evident in region II. The red dashed lines indicate the maximum $\Delta\tilde{x}_{sep}$ at the tilted angle $\alpha_{max}$.

In addition to diffraction effects of the SAW and BAW, the acoustically induced fluid flow, higher-order wave reflections, particle–particle interactions, anechoic corners, and the three-dimensional nature of the acoustofluidic separation, both in terms of the spatial distribution of focused particles and the acoustic pressure field, were neglected. These aspects are significantly influenced by the selection of the wavelength of the SAW, the channel geometry, and the channel material. To shed light on the impact of these parameters, comprehensive experimental and numerical investigations are combined in the following sections.

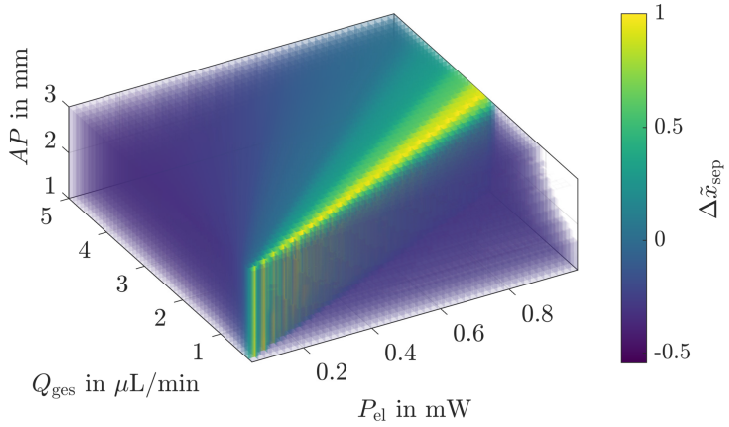


**Figure 7.** Three-dimensional representation of the normalized separation distance $\Delta\tilde{x}_{sep}$ achieved by varying the input power $P_{el}$, the volume flow rate $Q_{total}$, and the aperture $AP$. In the separation, particles with radii of 0.25 µm, 0.5 µm, and 2.5 µm were used.

### *3.2. Effect of the Acoustically Induced Fluid Flow*

A stationary fluid flow is excited due to the attenuation of the BAWs in the fluid, the so-called acoustic streaming effect [41]. This acoustically induced flow affects the motion of suspended particles via Stokes' drag and significantly impacts the focusing of particles

on pressure nodes. Following the comprehensive experimental and two-dimensional numerical investigations in Sachs et al. (2022) [51], the influence of the wavelength of the SAW $\lambda_{SAW}$ and the channel height $H$ on the flow pattern and velocity magnitude is analyzed briefly in the following. The interested reader is referred to Sachs et al. (2022) [51] for a more detailed discussion. Since the focusing of particles in the channel cross-section is of interest, experiments were performed in an acoustofluidic device with pressure nodes parallel to the channel side walls, i.e., $\alpha = 0°$. Furthermore, an aqueous glycerol mixture (80/20 $w/w$ deionized water/glycerol) with a density adapted to that of polystyrene particles was used as fluid to lower the acoustic contrast factor and achieve a high flow fidelity in the velocity measurements (see Section 2.2).

In Figure 8, measured and calculated flow patterns in the center of the sSAW are compared for different wavelengths of the SAW and channel heights. In all experiments, the width of the microchannel was kept constant at 500 µm. Although a higher separation distance is feasible with increasing channel width, the counter-propagating SAWs are attenuated more strongly and the acoustically induced fluid flow is enhanced [40]. By adapting crucial parameters in the numerical model, e.g., the acoustic impedance of PDMS and the speed of sound of the fluid, excellent agreement between experimental and numerical results was achieved both qualitatively and quantitatively [51]. A transition from vortex structures that extend far across the channel cross-section to periodic flow patterns can be identified with increasing wavelength and decreasing channel height. In the case of $\lambda_{SAW} = 150\,\mu m$ or $H = 85\,\mu m$, these vortices are spatially limited between two neighboring pressure nodes. This is advantageous for separation, as particles with a small radius or low acoustic contrast factor that tend to follow the fluid flow are not dispersed over the entire channel cross-section. A critical channel height $H_{crit} < \lambda_{SAW}/(2\tan\theta_{fluid})$ and width $W_{crit} < -ln(0.6)/C_d$ were derived from a structural analysis to obtain periodic flow patterns, using the Rayleigh angle $\theta_{fluid} = \arcsin(c_0/c_s)$ [51].

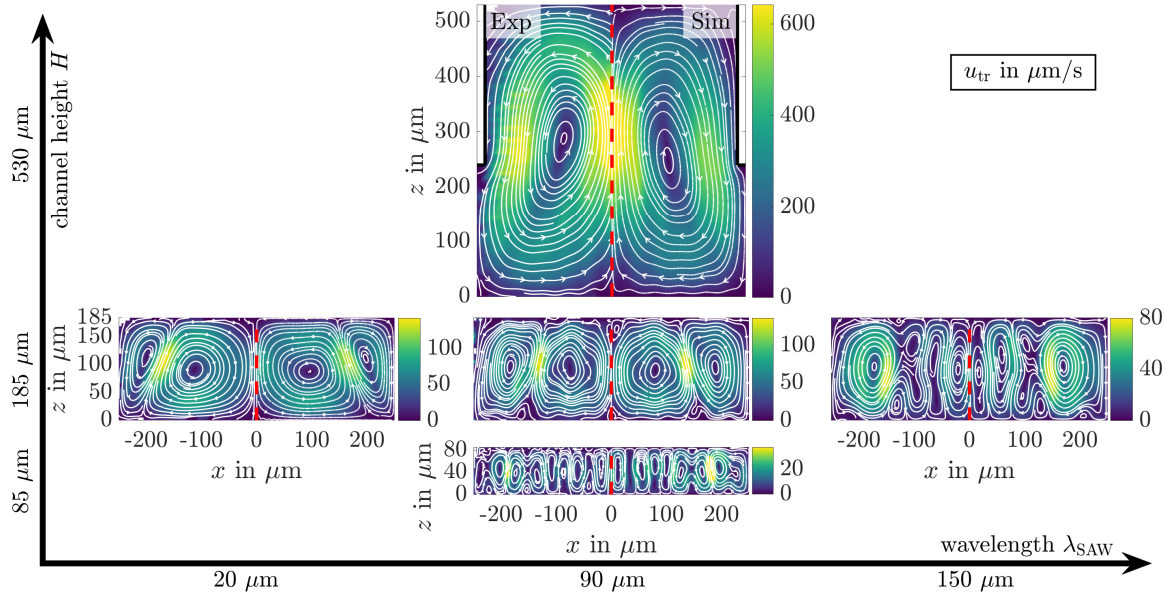


**Figure 8.** Experimentally (left half of the subfigures, $u_{tr} = \sqrt{u_x^2 + u_z^2}$) and numerically (right half of the subfigures, $u_{tr} = \sqrt{u_{2,x}^2 + u_{2,z}^2}$ using the second-order fluid velocity $\boldsymbol{u}_2$) derived time-averaged absolute velocity fields for varying wavelengths of the SAW $\lambda_{SAW}$ (horizontal) and channel heights $H$ (vertical). The acoustically induced fluid flow is indicated by white streamlines and the magnitude of $u_{tr}$ by colors. This figure is adapted from Sachs et al. (2022) [51].

Furthermore, the maximum flow velocity and kinetic energy density decrease with increasing wavelength and decreasing channel height due to a reduced attenuation of

the BAWs in the fluid and SAWs along the channel width. However, the influence of a decreasing channel height on the maximum fluid velocity revealed more significance within the investigated parameter range. Moreover, wavelength-dependent attenuation losses of the SAW are significant, which mainly occur due to the influence of the channel side walls and were taken into account by means of a decreasing coupling factor $k_\eta$ (see Table 1) in the numerical model. These losses are not included in the fundamental dependency of $\boldsymbol{F}_{\mathrm{rad}}$ on the wavelength and represent an important aspect in the design of acoustofluidic separation devices. The lower energy loss of the SAW at the side walls with increasing wavelength manifests itself in an increasing acoustic energy density, which offers advantages for particle separation. By increasing the wavelength and reducing the channel height, the acoustically induced fluid flow is thus suppressed, while the influence of $\boldsymbol{F}_{\mathrm{rad}}$ on the behavior of the particles increases.

**Table 1.** Coupling factor $k_\eta$ for different configurations of the wavelength of the SAW $\lambda_{\mathrm{SAW}}$ and channel height $H$ obtained by combining experimental and numerical results [51].

| **Wavelength** $\lambda_{\mathrm{SAW}}$ | **Channel Height** $H$ | **Coupling Factor** $k_\eta$ |
|---|---|---|
| 20 µm | 185 µm | 0.0073 |
| 90 µm | 85 µm | 0.4196 |
| 90 µm | 185 µm | 0.4427 |
| 90 µm | 530 µm | 0.3730 |
| 150 µm | 185 µm | 0.5782 |

The relative dominance of $\boldsymbol{F}_{\mathrm{rad}}$ and $\boldsymbol{F}_{\mathrm{drag}}$ in the channel cross-section $S$, which can be quantified using the mean force coefficient $\psi = \langle |\boldsymbol{F}_{\mathrm{rad}}| / |\boldsymbol{F}_{\mathrm{drag}}| \rangle_S$ [51], is key for the focusing and separation of suspended particles. Resulting from the linear and cubic relationships of $\boldsymbol{F}_{\mathrm{drag}}$ and $\boldsymbol{F}_{\mathrm{rad}}$ to the particle radius $r$, respectively, $\psi$ scales quadratically with $r$ (see Figure 9). Hence, the focusing of particles with smaller radius appears challenging under the influence of the acoustically induced fluid flow. A critical particle radius $r_{\mathrm{crit}}$ is derived as $\boldsymbol{F}_{\mathrm{rad}}$ and $\boldsymbol{F}_{\mathrm{drag}}$ compensate on average, i.e., $\psi \equiv 1$ (see inset in Figure 9). As a consequence of the decreasing kinetic and increasing acoustic energy density, the critical particle radius decreases with increasing wavelength and decreasing channel height in the analyzed parameter range. Thus, shallow microchannels and large wavelengths are advantageous for the separation of particles with small radii or low acoustic contrast factors.

Focusing the particles on pressure nodes in the channel cross-section is essential for separation. However, in order for the particles to follow the pressure nodes of an tas-SAW, the Stokes' drag due to the superimposed main flow must further be considered. In Figure 9b, the average force difference $\Delta F = \langle |F_{\mathrm{rad,x'}}| - |F_{\mathrm{drag,y}}| \sin\alpha \rangle_S$ in the $x'$-direction is plotted for different wavelengths versus the channel height. In the calculation, the velocity distribution in the microchannel was derived analytically [72], and the tilted angle was set to $\alpha_{\mathrm{max}}$. When $\Delta F$ turns positive, $|F_{\mathrm{rad,x'}}|$ dominates over $|F_{\mathrm{drag,y}}| \sin\alpha$ on average, and the particles follow the pressure nodes with a higher probability. As the channel height decreases, the main flow velocity increases at a constant volume flow rate and $\Delta F$ drops. Consequently, a conflict of objectives arises, which sets a lower limit regarding the channel height. Furthermore, distinct peaks with a distance $\Delta z$ occur in the course of $\Delta F$. In rectangular channel geometries with $W = \lambda_{\mathrm{SAW}}/2$, this distance was found to coincide with $\Delta z = \lambda_0/2$ [79], where $\lambda_0$ is the wavelength of the BAW propagating in the undisturbed fluid. However, an irregular trend is evident from Figure 9b, as typical for a channel width $W > \lambda_{\mathrm{SAW}}/2$, featuring significantly more complex pressure and velocity fields [80]. Based on the numerical results, microchannels with channel heights corresponding to peaks in $\Delta F$ are beneficial for the acoustofluidic particle separation. Furthermore, higher peaks in $\Delta F$

are achieved using a SAW wavelength of $\lambda_{SAW} = 90\,\mu m$, while the critical particle radius remained similar to using $\lambda_{SAW} = 150\,\mu m$. Hence, the greater acoustic radiation force allows for the precise manipulation of spherical particles with radii $r > r_{crit}$ at higher throughput.

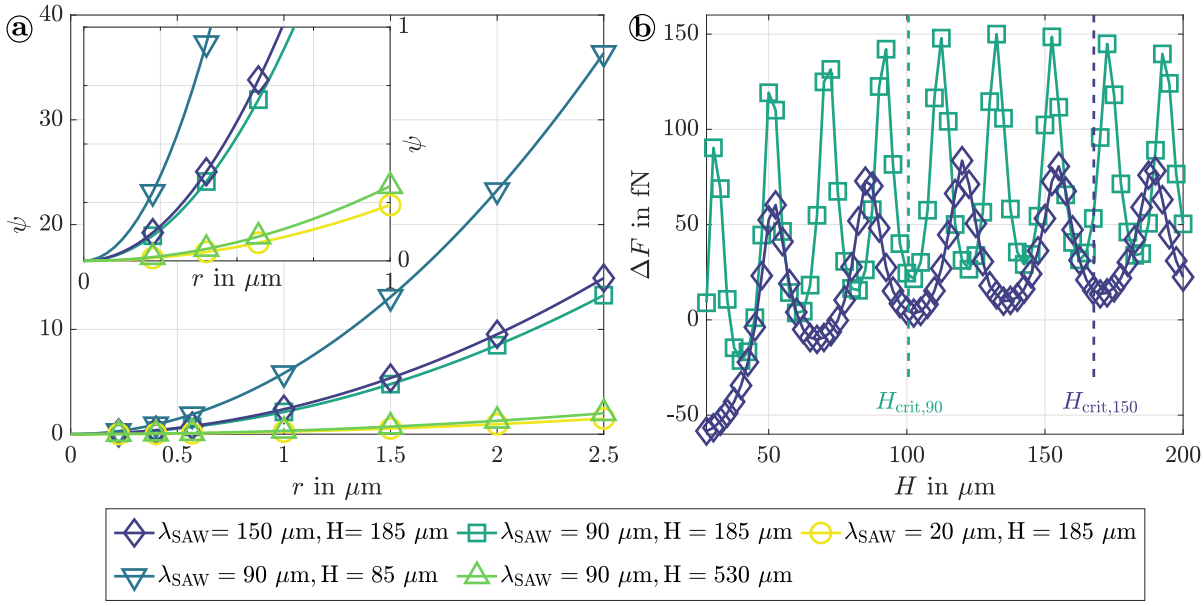


**Figure 9.** Mean force coefficient $\psi$ against the particle radius $r$ for different configurations of ($\lambda_{SAW}$, $H$) (**a**). The course of $\psi$ up to a particle radius of $r = 1\,\mu m$ and $\psi = 1$ is shown in the inset. The numerical data were linked by quadratic regression. This subfigure was adapted from Sachs et al. (2022) [51]. Average force difference $\Delta F$ as a function of the channel height $H$ for wavelengths of 90 µm and 150 µm with the corresponding critical channel heights $H_{crit,90}$ and $H_{crit,150}$ highlighted by dashed lines (**b**). The volume flow rate and electrical power were set constant at $Q_{total} = 0.03\,\mu L\,min^{-1}$ and $P_{el} = 20\,mW$, respectively.

### *3.3. Three-Dimensional Nature of the Particle Separation*

The particle separation in acoustofluidic devices is three-dimensional in nature, which is reflected in the stable focus positions of the particles. Based on experimental results, two key aspects influencing the separation result are considered below and incorporated in a three-dimensional numerical model to calculate the particle trajectories precisely: (i) The acoustically induced fluid flow in the outer regions of the sSAW field and (ii) the focusing of particles at different height levels.

(i) Strong gradients in the displacement amplitude of the sSAW are evident at the beginning and end of the aperture of the IDTs. These gradients translate into the acoustic fields within the fluid domain and generate a body force that drives three-dimensional, acoustically induced vortex structures in the outer regions. In Figure 10a,c, the experimentally observed patterns of the fluid flows at the beginning and end of the sSAW are depicted for a SAW wavelength of $\lambda_{SAW} = 20\,\mu m$, respectively [54]. Due to the interaction with the pressure-driven main flow, the vortices form near the channel ceiling at the beginning and near the bottom at the end of the sSAW. Consequently, the fluid velocity in the main flow direction ($y$) increases locally. Furthermore, the acoustically induced vortex structures might influence the particle trajectories during separation. In particular, there is a risk of lateral displacement of pre-positioned particles at the beginning and remixing of already separated particles at the end of the sSAW. Based on a comprehensive experimental analysis of the fluid flow, the use of large wavelengths of the sSAW and low channel heights is found to reduce the influence of the induced vortices. For a detailed discussion, the interested reader is referred to Sachs et al. (2022) [54]. To improve the design of acoustofluidic devices based on the revealed fundamental dependencies, a three-dimensional numerical model

was set up to calculate the fluid flow. In Figure 10b,d, the numerically calculated velocity fields at the beginning and end of the sSAW are illustrated by streamlines, respectively. To limit the numerical effort, the wavelength was increased to $\lambda_{SAW} = 90\,\mu m$. Furthermore, the surface displacement $A$ by the sSAW was specified analytically as a boundary condition at the channel bottom without variation in the $y$-direction [51]. Hence, gradients in $A$ are overestimated in the outer regions. However, the numerical results indicate an excellent agreement with the patterns of the experimentally detected vortices. Consequently, the numerical model allows for the integration of the influence of the acoustically induced fluid flow on the particle trajectories in a flexible manner as described below.

(ii) The pattern of the acoustic pressure field within a microchannel made of PDMS with a height $H \geq \lambda_f/2$ features multiple nodes and antinodes along the channel height where particles can be focused. Hence, the particle separation in a tasSAW device is translated into a three-dimensional process, as demonstrated in Figure 11 by the separation of particles with radii of 4.94 µm, 2.52 µm, and 0.57 µm. According to the scaling of the acoustic radiation force with the volume of the particles, the trajectories of the smallest particles are almost unaffected. However, contrary to the result obtained with the simplified semi-analytical model (see Figure 4a), some of the medium-sized particles with $r = 2.52\,\mu m$ are more strongly displaced across the channel width than the largest particles, as can be seen in the top view in Figure 11a. The reason for this unexpected behavior can be found in the arrangement of the particles in two height levels, as shown in the channel cross-section in Figure 11b. While the 4.94 µm particles are positioned close to the midplane of the channel, the other particles are additionally located close to the channel ceiling. Here, the fluid velocity of the main flow is significantly lower than in the middle plane due to no-slip boundary conditions at the ceiling. As a consequence, the acoustic radiation force dominates the particle trajectories near the channel ceiling, while the drag force due to the main flow determines the particle motion in the middle plane. Resulting from the different regimes, a separation of the targeted particle solution is not conceivable with high purity in the investigated device. To circumvent the focusing to different height levels, the channel height may be reduced to $H < \lambda_f/2$. However, the main flow velocity increases simultaneously at a constant volume flow rate, which imposes limits on the throughput. Another approach is to incorporate a channel ceiling with high acoustic impedance to promote reflections of the acoustic waves and increase the acoustic energy density [35,81] as well as to force a symmetric positioning of the pressure nodes w.r.t. height.

To assess the influence of a channel ceiling with high acoustic impedance, a three-dimensional numerical model of a tasSAW device was used. In Figure 12a,b, calculated trajectories of the spherical polystyrene particles are depicted for a microchannel with a channel ceiling made of PDMS ($Z_{PDMS} = 1.04 \times 10^6\,Pa\,s\,m^{-1}$ [82]) or silicon (Si, $Z_{Si} = 19.79 \times 10^6\,Pa\,s\,m^{-1}$ [59]), respectively. The normalized surface displacement $\tilde{A}$ by the sSAW was reconstructed based on measurements of a traveling SAW and set as boundary condition at the channel bottom [57]. In this way, gradients in $\tilde{A}$ in the outer regions and diffraction effects of the SAWs are taken into account. In the case of the ceiling made of PDMS, the particles are forced to pressure minima near the channel bottom, ceiling, and middle plane as indicated by the final particle positions in the channel cross-section depicted in Figure 12c. Due to the different fluid velocities in these height levels, the lateral displacement of the particle is significantly increased near the channel ceiling. In accordance with the experimental results, a particle separation with low purity would result. Furthermore, the numerically calculated lateral displacement of particles located near the channel bottom is significantly lower than near the ceiling due to the pattern of the acoustic fields. However, no particles were found near the channel bottom in the experiment. The reason could be given by the piezoelectric effect, which is why the sSAW is inherently

accompanied by an electric field that levitates the particles by a dielectrophoretic force [58]. This was not considered in the numerical model. In the case of a ceiling made from silicon, the amplitude of the time-averaged absolute acoustic pressure field $\langle|p_1|\rangle$ increases by a factor of approx. three (see Figure 12d). Furthermore, $\langle|p_1|\rangle$ possesses a more regular pattern with pressure nodes located almost symmetrically to the midplane of the channel ($H/2$). As a result, the particles are focused on height levels where a comparable flow velocity is present in the main flow direction ($y$). Hence, the lateral displacement of the particles at the different height levels appears similar. Based on the numerical model, a pure separation of the particle solution is achieved due to the size-selective lateral displacement of the particles in the proposed channel design.

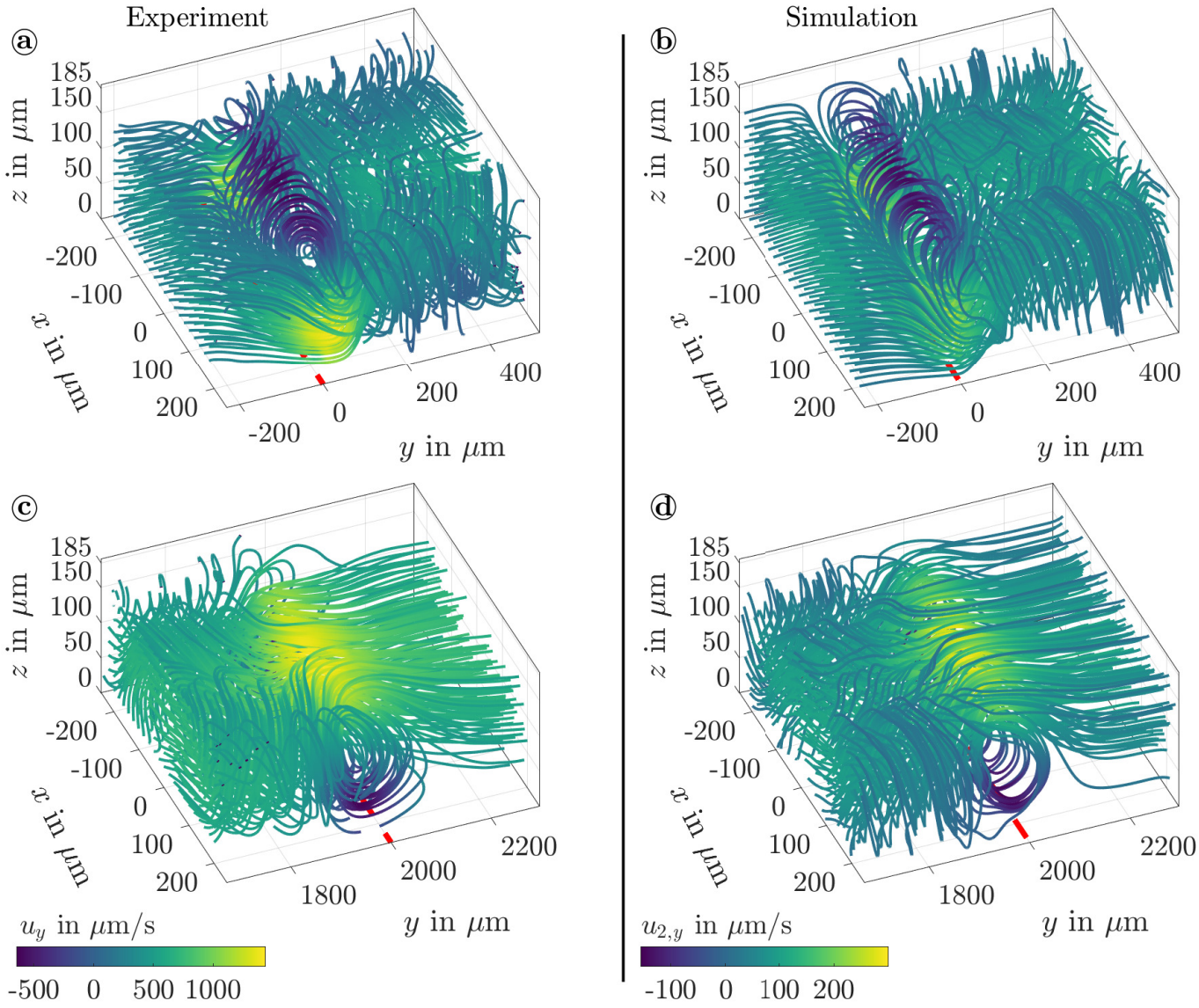


**Figure 10.** Experimental results on the velocity field near the beginning (**a**) and end (**c**) of the IDTs, which are marked by red dashed lines ($\lambda_{SAW} = 20\,\mu m$, $H = 185\,\mu m$, $P_{el} = 154\,mW$, $Q_{total} = 1.6\,\mu L\,min^{-1}$). These subplots were adapted from [54]. In (**b**,**d**), the acoustically induced vortices are calculated numerically in the same regions ($\lambda_{SAW} = 90\,\mu m$, $H = 185\,\mu m$, $P_{el} = 29.8\,mW$, $Q_{total} = 0.33\,\mu L\,min^{-1}$). The streamlines are colored in correspondence to the velocity component $v$ in main flow direction.

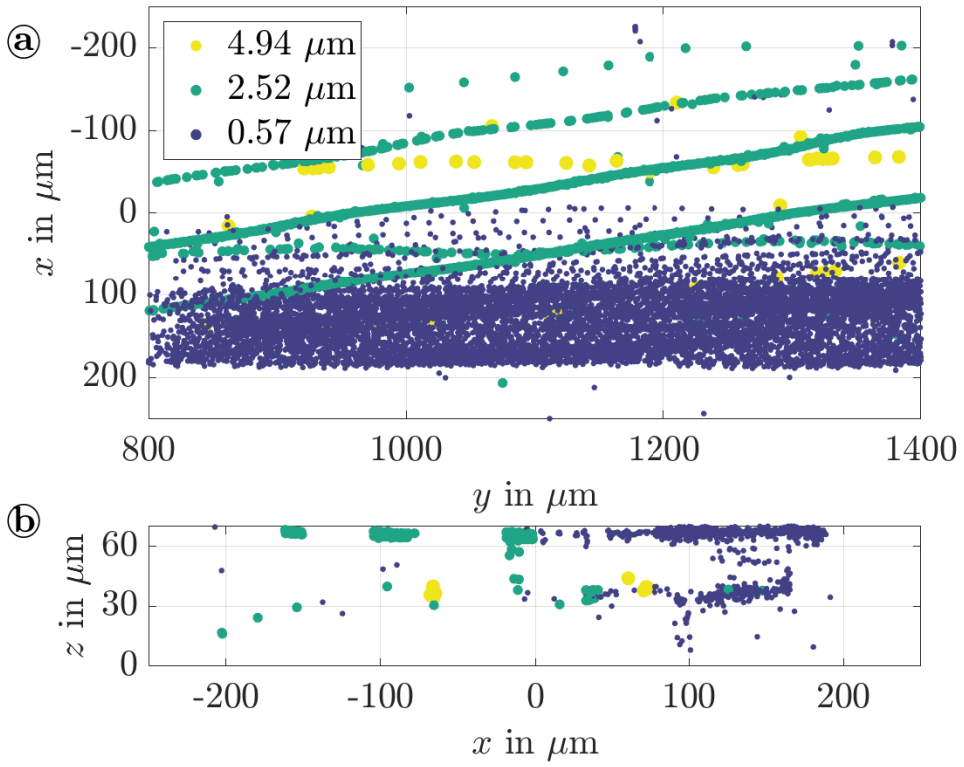


**Figure 11.** Measured positions of particles with radii of 4.94 µm, 2.52 µm, and 0.57 µm from a top view (**a**) and in the channel cross-section (**b**) of the tasSAW device ($\lambda_{SAW} = 150\,\mu m$, $H = 70\,\mu m$, $P_{el} = 285\,mW$, $Q_{total} = 4.6\,\mu L\,min^{-1}$). A main flow was applied in positive *y*-direction.

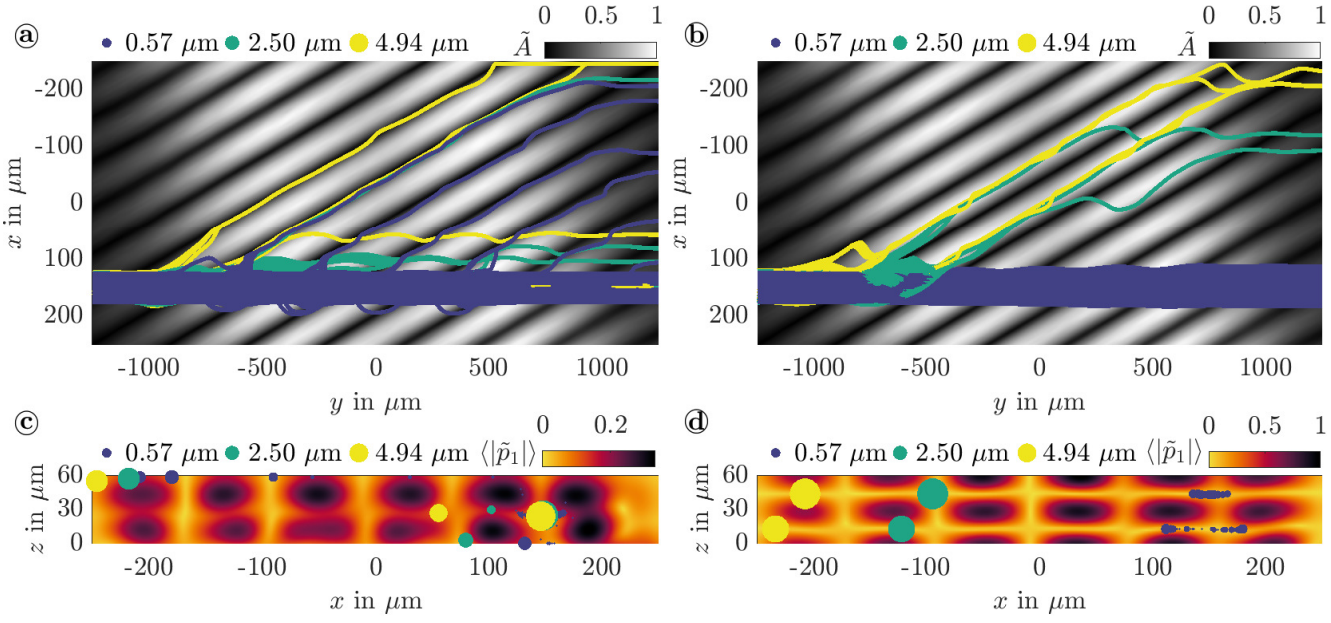


**Figure 12.** Particle trajectories calculated in a three-dimensional numerical model with a channel ceiling made of PDMS (**a**,**c**) at $\lambda_{SAW} = 150\,\mu m$, $H = 60\,\mu m$, $P_{el} = 285\,mW$, and $Q_{total} = 5.7\,\mu L\,min^{-1}$ or silicon (**b**,**d**) at $Q_{total} = 6.5\,\mu L\,min^{-1}$. The normalized amplitude $\tilde{A}$ of the tasSAW used as boundary condition is depicted in (**a**,**b**). The final particle positions at the end of the computational domain are illustrated against the normalized time-averaged absolute acoustic pressure field $\langle|\tilde{p}_1|\rangle$ in the channel cross-section in (**c**,**d**). The size of the dots corresponds to the number of particles found in the respective location.

The numerically calculated focusing of particles at different height levels was verified based on an experiment using an acoustofluidic device with a ceiling and side walls made of silicon and dry film resist, respectively. Details on the fabrication of the device can be found in Appendix B. In the experiment, polystyrene particles with a radius of 1.25 µm were suspended in deionized water and pumped through the microchannel with a height of approx. 60 µm. As depicted in Figure 13a, the randomly distributed particles were focused into discrete clusters in the channel cross-section by means of the acoustic pressure field stemming from the sSAW. In line with the numerical results, about 83.75 % of the particles were located at height levels of $z_1 = H/4 \pm 5\,\mu\text{m}$ or $z_2 = 3H/4 \pm 5\,\mu\text{m}$, which is further emphasized by the corresponding probability density function (pdf) in Figure 13b. Hence, only a small fraction of about 16.25 % of the particles was positioned outside $z_1$ or $z_2$, where the fluid velocity in the main flow direction differed significantly. According to the experimental and numerical findings, the proposed design of the acoustofluidic devices using a channel ceiling of high acoustic impedance revealed to be highly beneficial for a selective and efficient particle separation.

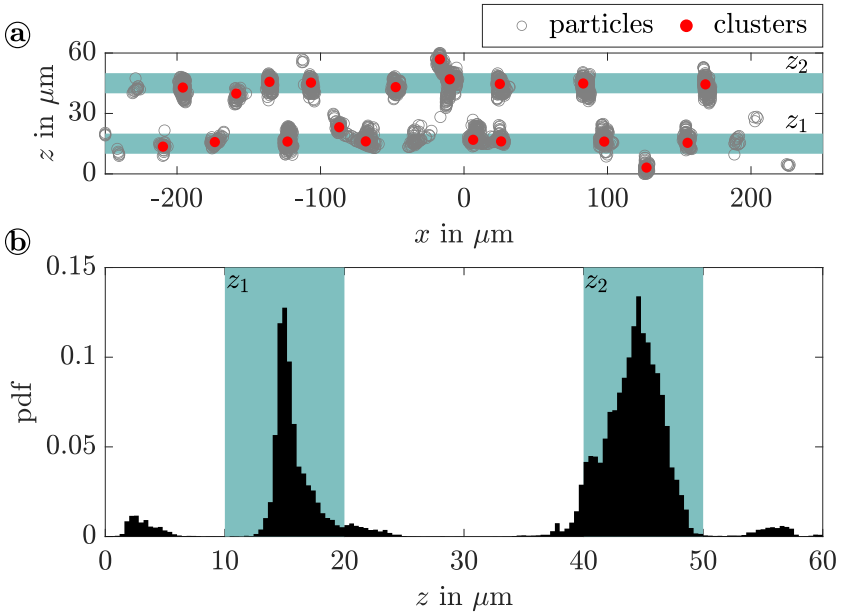


**Figure 13.** Measured locations of particles forming clusters at discrete focus positions in the channel cross-section (**a**). These clusters are located mainly at the two height levels, $z_1$ and $z_2$. In (**b**), the distribution of the detected particles is depicted as a function of the depth position $z$ in a histogram.

### *3.4. Shape-Dependent Particle Separation*

The separation of particles in tasSAW-based devices is dominated by the acoustic radiation force, which scales with the particle volume and acoustic contrast factor. However, according to Equation (1), the acoustic radiation force is calculated by gradients in the incident and scattered acoustic fields. If a suspended particle covers significant acoustic gradients, not only the acoustic radiation force but also an acoustic torque exerts on the particles depending on the particle shape and orientation [83]. Using the relation between the acoustic radiation force and the particle shape, an acoustofluidic separation by particle shape is feasible, as demonstrated by Khan et al. (2024) using traveling SAWs [84]. To reveal differences in the acoustic force acting on particles of different shapes, the dynamic behavior of prolate polystyrene spheroids was analyzed in a pseudo-standing acoustic pressure field with multiple pressure nodes along the channel width. The non-spherical particles were prepared from fluorescence-labeled spherical polystyrene particles (PS-FluoRed, MicroParticles GmbH, $r = 2.501\,\mu\text{m}$) in a stretching process [85] (see Figure 14a).

Exploiting the rotational symmetry of the particles, the kinematic behavior is analyzed by evaluating the position $(x, y, z)$ and orientation $(\varphi, \theta)$ over time (see Figure 14b).

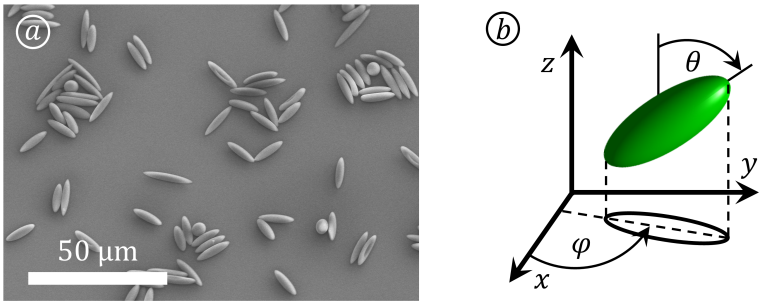


**Figure 14.** Prolate spheroids dried on a silicon wafer and recorded by scanning electron microscopy (**a**). The position $(x, y, z)$ and orientation $(\varphi, \theta)$ of the non-spherical particles is defined in the coordinate system given in (**b**), which was adapted from Sachs et al. (2023) [57].

Without the influence of the sSAW, the transient behavior of the particles suspended in a pressure-driven microflow is determined by tumbling, logrolling, and kayaking [55,86–90]. This is reflected in a broad distribution of the detected in-plane angle $\varphi$ as illustrated in Figure 15a. However, the particles prefer to align their major axis in the main flow direction ($\varphi = 90°$). Under the influence of the pseudo-standing acoustic wave field, the transient rotation is suppressed, and the particles prefer an orientation orthogonal to the main flow direction ($\varphi = 180°$), as indicated by a clear peak in Figure 15a. Hence, the particles are aligned perpendicular to the pressure nodes and, therefore, parallel to the propagation direction of the SAWs, while an orientation perpendicular to the propagation direction was typically found in previous studies with different design parameters [84,91–97]. By combining the experimental results with a numerical analysis, not only was the in-plane orientation confirmed, but also an out-of-plane orientation $\theta$ at about 50.36° or 136.35° was found [58]. This unintuitive orientation of the particles is predominantly determined by the pattern of the acoustic fields. In addition to the acoustic torque, a dielectrophoretic torque is exerted on the polarizable particles due to the inhomogeneous electric field that accompanies the sSAW. However, it was shown experimentally and numerically that both torques apply complementarily to align the particles at $\varphi = 180°$ [58]. Compared with the acoustic force, the dielectrophoretic force contributes only marginally to the lateral displacement of the particles. As depicted in Figure 15b, the non-spherical particles are focused to stable positions with a distance of approx. $\lambda_{SAW}/2$ along the channel width. Hence, similar to spherical particles, the prolate spheroids are forced into a discrete pattern by the acoustic force.

Based on a three-dimensional numerical model, the acoustic force was integrated across the equilibrium surface of a particle modeled within the fluid domain. Following the numerical approach, a potential separation of a spherical particle and prolate spheroid oriented at $(\varphi = 0°, \theta = 90°)$ with identical volume was investigated. Due to the promising results on the particle separation in a microchannel with a ceiling of high acoustic impedance (see Section 3.3), the channel cover was designed of glass with an acoustic impedance of $Z_{glass} = 12 \times 10^6\,\mathrm{Pa\,s\,m^{-1}}$. In Figure 16a, the normalized acoustic force component $\tilde{F}_x$ acting on the spherical and non-spherical particle is depicted along the $x$-position for a shift between two neighboring pressure nodes (PN). For both particles, the acoustic force takes positive/negative values on the left/right side of the antinode (AN) of the acoustic pressure field, respectively. Hence, the particles are pushed to a stable position in the pressure minima between neighboring antinodes along the channel height (see Figure 16b). To separate the particles in a tasSAW device, differences in the maximum acoustic force are crucial for the particles to selectively follow the pressure nodes. In the

given design of the acoustofluidic device, the acoustic force applied to the prolate spheroid exceeds the force exerted on the spherical particle by approx. 19.8 %. Consequently, the separation of the isovolumetric particles according to their shape is feasible, rendering the acoustofluidic separation multidimensional in the separation criteria, including the particle size, acoustic contrast factor, and particle shape.

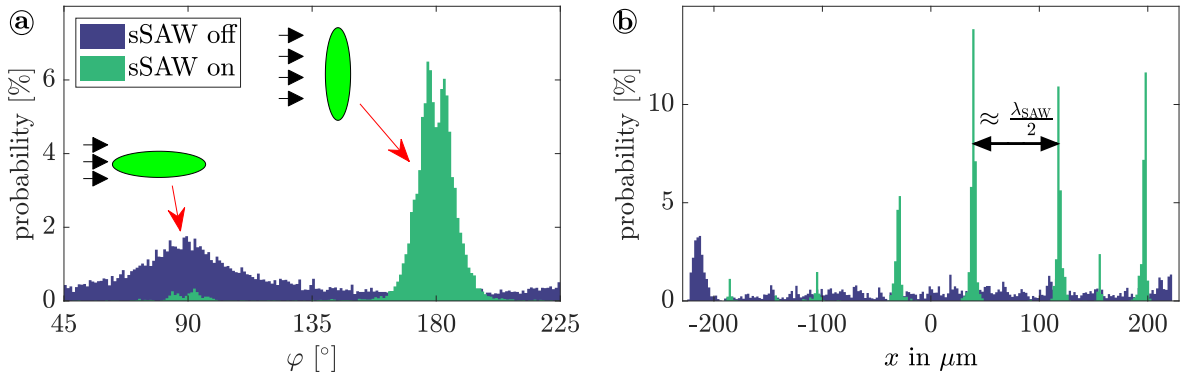


**Figure 15.** Relative frequency of the detected in-plane angle $\varphi$ (**a**) and position $x$ of particles along the channel width (**b**). The preferred orientation of the prolate spheroids with and without the influence of the sSAW is indicated by green ellipses with the main flow direction indicated by black arrows. This figure was adapted from Sachs et al. (2023) [57].

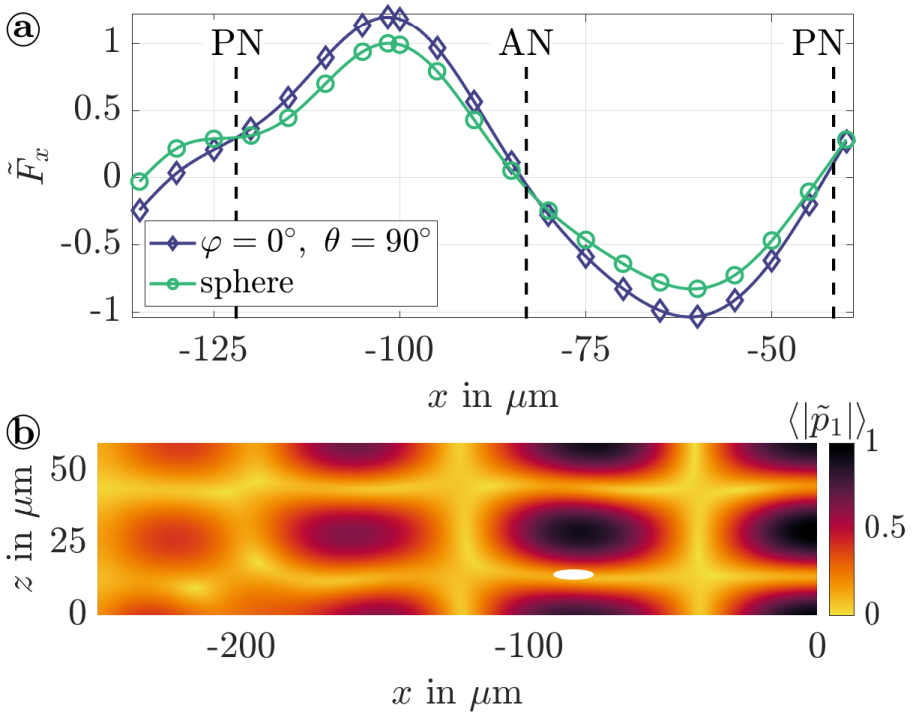


**Figure 16.** Normalized acoustic force component $\tilde{F}_x$ acting on a prolate spheroid and a sphere of identical volume against the $x$-position (**a**). The numerically calculated data are fitted by smoothing splines. Normalized time-averaged absolute acoustic pressure $\langle|\tilde{p}_1|\rangle$ in half the channel cross section with the prolate spheroid depicted at a stable position (**b**). This figure was adapted from Sachs et al. (2023) [57].

## 4. Conclusions

Within this project, physical phenomena governing the multidimensional separation of particles of different sizes, shapes, and materials, which result in different acoustic contrast factors, were examined using tilted-angle standing surface acoustic wave (tasSAW) devices.

By applying experimental, semi-analytical, and numerical methods, the influence of control and design parameters on the multiphysical phenomena governing the separation process was investigated. In this way, the following guidelines to design the acoustofluidic device for a tailored particle separation were derived:

- By using the maximum **tilt angle**, which allowed the particles to reach the opposite channel side wall at the end of the tasSAW, an increasing separation distance of multiple particle species in a suspension was achieved. However, a lower tilt angle revealed beneficial for a higher throughput with limited electrical input power.
- As the **wavelength of the SAW** $\lambda_{SAW}$ increases, the acoustically induced fluid flow transitions to periodic flow patterns with lower fluid velocities, essential to focus suspended particles in pressure nodes. As a result, the critical size of particles predominantly manipulated by the acoustic radiation force decreased with increasing $\lambda_{SAW}$ in the investigated range.
- A similar transition of flow patterns was found with decreasing **channel height** $H$. Based on a structural analysis, a critical channel height $H_{crit}$ and width $W_{crit}$ were derived for the design of acoustofluidic separation devices based on sSAWs. Moreover, clear peaks in the force difference $\Delta F$ between the acoustic radiation force and Stokes' drag due to the pressure-driven main flow were identified as a function of the channel height $H$. Hence, a selection of the appropriate channel height corresponding to peaks in $\Delta F$ revealed beneficial.
- Dealing with the three-dimensional nature of the acoustofluidic particle separation, a **channel material** with high acoustic impedance at the ceiling of the microchannel revealed beneficial. The enhanced wave reflection not only yielded a significantly increased acoustic energy density but also allowed a particle distribution symmetrically to $H/2$, where a similar Stokes' drag due to the main flow occurred.

Consequently, a distinct particle separation is feasible based on results obtained by a three-dimensional numerical model to calculate the trajectories of particles within the pseudo-standing acoustic wave field.

Making use of the derived design guidelines, a difference of about 19.8 % in the acoustic force acting on a prolate spheroid and a sphere with identical volume was further calculated. Hence, a shape-dependent separation is conceivable, which qualifies the tasSAW-based device as a multidimensional separation technology of particles according to size, shape, and acoustic contrast factor.

In subsequent studies, the experimental implementation of the shape-dependent separation as well as highly specific and multidimensional particle separation in the modified channel design is feasible. A promising approach to fabricate this acoustofluidic device is found in the use of dry film resists. These photoresists allow for lithographic precision in the positioning and shape of the microchannels with the option to fine-tune the channel height [98]. Furthermore, the greater flexibility in the selection of the channel ceiling material enables an enhanced acoustic wave reflection by using silicon or glass with high acoustic impedance [81]. Based on the numerical and experimental studies, a transition from the widely used PDMS-based microchannels to the proposed channel design enables the establishment of tasSAW-based devices as a promising technology for multidimensional particle separation.

**Author Contributions:** Conceptualization, S.S., J.K. and C.C.; methodology, S.S., J.K. and C.C.; software, S.S.; validation, S.S.; formal analysis, S.S.; investigation, S.S.; resources, J.K. and C.C.; data curation, S.S.; writing—original draft preparation, S.S.; writing—review and editing, S.S., J.K. and C.C.; visualization, S.S.; supervision, J.K. and C.C.; project administration, J.K. and C.C.; funding acquisition, J.K. and C.C. All authors have read and agreed to the published version of the manuscript.

**Funding:** This research was funded by the German Research Foundation (DFG) within the priority program PP2045 "MehrDimPart" under grant number 444806275.

**Institutional Review Board Statement:** Not applicable.

**Informed Consent Statement:** Not applicable.

**Data Availability Statement:** The data sets that support the findings of this study are available from the corresponding author, S.S., upon request.

**Acknowledgments:** The authors thank the German Research Foundation (DFG) for financial support within the priority program PP2045 "MehrDimPart" (444806275). Support by the Center of Micro- and Nanotechnologies (ZMN) (DFG RIsources reference: RI_00009), a DFG-founded core facility of TU Ilmenau, is gratefully acknowledged. Furthermore, we thank Laura Weirauch (University of Bremen), who supported non-spherical particles. Technical support by Henning Schwanbeck using the high-performance computing cluster at the Universitätsrechenzentrum of TU Ilmenau is gratefully acknowledged.

**Conflicts of Interest:** The authors declare no conflict of interest.

## Appendix A. Details on the Numerical Models

The two-dimensional numerical model covered the channel cross-section of height $H$ and width $W$ as depicted in Figure A1. To resolve the thin thermoviscous boundary layers, the quadrilateral elements forming the mesh were reduced in thickness by a factor of 1.2 in 10 to 15 layers adjacent to the boundaries. The first layer directly at the channel boundaries had a thickness of $0.3\delta$, where $\delta$ is the thickness of the viscous boundary layer. A detailed mesh independence study can be found in our previous work [51] using the same numerical model. Impedance boundary conditions were set at the fluid–PDMS interfaces to calculate the first-order fields. Furthermore, the first-order velocity was prescribed in the $z$-direction at the channel bottom, while a slip condition was set for the longitudinal displacement velocity by the sSAW in the $x$-direction. In the calculation of the second-order fields, no-slip boundary conditions were set at all channel boundaries.

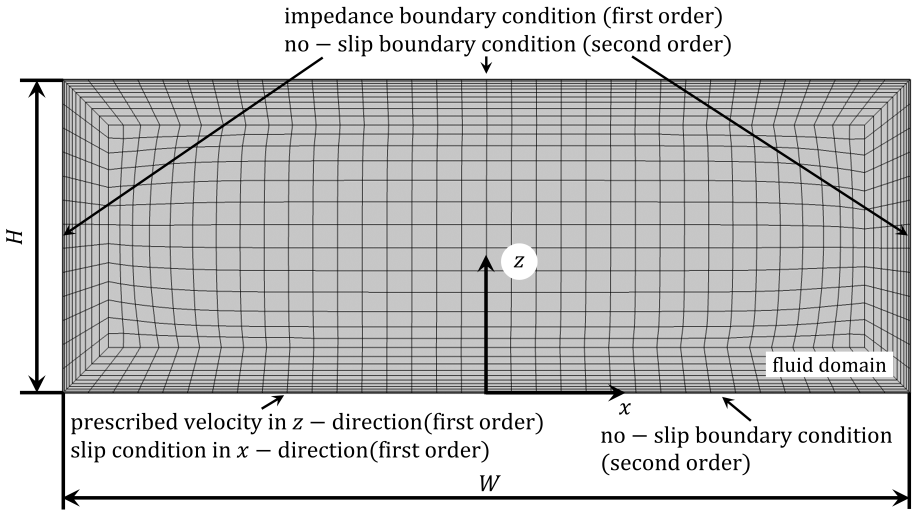


**Figure A1.** Computational mesh covering the channel cross section in the two-dimensional numerical model in a coarse configuration for visualization. Boundary conditions applied to calculate the first- and second-order field quantities are highlighted. This figure was adapted from [51].

In Figure A2a, the three-dimensional computational domain comprising the fluid within the acoustofluidic device is depicted schematically. To reduce the numerical effort, only half of the channel cross-section and 1.6 mm in the $y$-direction were resolved numerically. Symmetry conditions were set at the $yz$-plane at $x = 0$ and the $xz$-plane

at $y = AP/2$. Furthermore, the fluid–PDMS interfaces were represented by impedance boundary conditions to calculate the first-order field quantities and by no-slip boundary conditions for the second-order velocity field. At the inlet of the channel, i.e., at the $xz$-plane at $y = -600\,\mu m$, perfectly matched layers (PML, [99]) were included as boundary condition to calculate the first-order fields and an open boundary condition to compute the second-order fields. The surface-normal displacement velocity of the sSAW was prescribed as boundary condition at the channel bottom based on the temporal derivative of the sSAW displacement measured with an ultrahigh-frequency laser Doppler vibrometer (UHF-120, Polytec, Hörsching, Austria). Further details on the applied boundary conditions and material properties can be found in our previous work [57]. To calculate the acoustic force acting on a prolate spheroid within the fluid domain, the non-spherical particle was modeled as a solid domain within the fluid. As shown schematically in Figure A2b, continuity between the fluid and solid domains was enforced by setting an "Acoustic-Structure Boundary" [63] on the particle surface. To correctly capture the elastic deformation of the particle made of polystyrene, the prolate spheroid was modeled as a linear elastic solid [100].

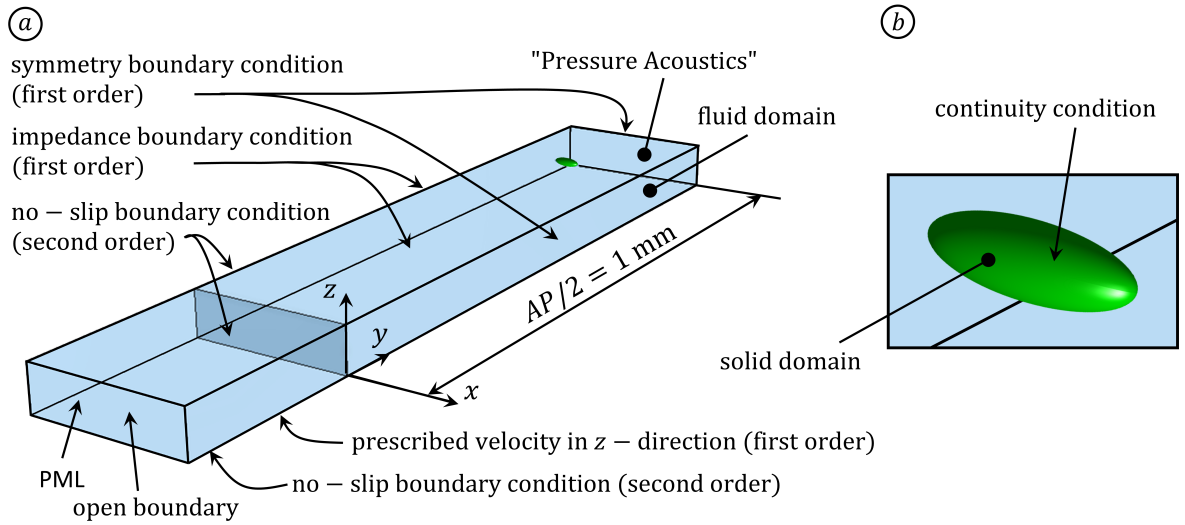


**Figure A2.** Three-dimensional numerical model along with the imposed boundary condition to calculate the first- and second-order quantities in a schematic representation (**a**). A detailed view on the prolate spheroid modeled as a solid domain within the fluid is given in subfigure (**b**). This figure was adapted from [57].

## Appendix B. Fabrication of the Acoustofluidic Device

The acoustofluidic device is based on a substrate of 128° rotated Y-cut lithium niobate ($LiNbO_3$), on which two opposing IDTs are deposited as described in Section 2.1. On top of the substrate, the dry film resist (DFR) Ordyl® SY300 was laminated and patterned by lithography to obtain the channel side walls with a height of 60 µm. To seal the microchannel, a cover made of silicon (Si, ⟨100⟩) with fluid inlets was used. By spin coating a thin layer of SU-8 photoresist with a thickness of about 3 µm onto the silicon substrate, a low-temperature bonding process on a chip level at 65 °C and applying approx. 90 N was established. In this way, the significant differences between the substrates in terms of the anisotropic thermal expansion and wafer bow were considered in the bonding process to achieve a sealed joint. Since the wavelength of the BAWs traveling in the fluid is significantly greater than the thickness of the SU-8 layer at the channel ceiling, the high reflection at the SU-8/silicon interface is expected to dominate the distribution of the acoustic fields in the fluid. This assumption is further strengthened by the focusing of particles at height levels symmetrically to $H/2$ as predicted by the numerical model (see Section 3.3).

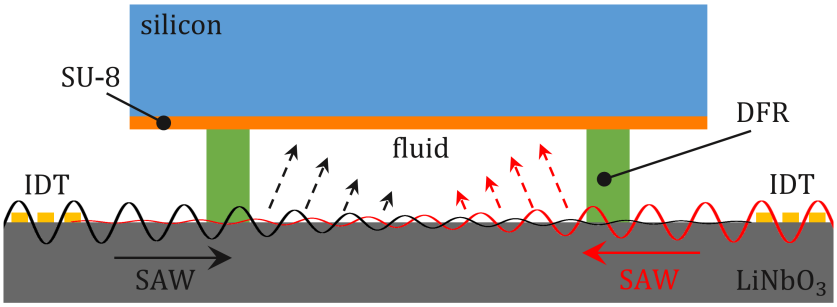


**Figure A3.** Schematic representation of the acoustofluidic device in a cross-sectional view. Counter-propagating SAWs are excited by two opposing IDTs, which radiate energy into the fluid-filled microchannel consisting of side walls made of DFR and a channel cover of silicon.

## References


1. Sajeesh, P.; Sen, A.K. Particle separation and sorting in microfluidic devices: A review. *Microfluid. Nanofluid.* **2014**, *17*, 1–52. [CrossRef]
2. Li, M.; Li, W.H.; Zhang, J.; Alici, G.; Wen, W. A review of microfabrication techniques and dielectrophoretic microdevices for particle manipulation and separation. *J. Phys. D Appl. Phys.* **2014**, *47*, 063001. [CrossRef]
3. Patel, S.; Qian, S.; Xuan, X. Reservoir-based dielectrophoresis for microfluidic particle separation by charge. *Electrophoresis* **2013**, *34*, 961–968. [CrossRef] [PubMed]
4. Ahmad, M.; Bozkurt, A.; Farhanieh, O. Evaluation of acoustic-based particle separation methods. *World J. Eng.* **2019**, *16*, 823–838. [CrossRef]
5. Zhu, G.; Nguyen, N.T. Particle Sorting in Microfluidic Systems. *Micro Nanosyst.* **2010**, *3*, 202–216. [CrossRef]
6. Volpe, A.; Gaudiuso, C.; Ancona, A. Sorting of Particles Using Inertial Focusing and Laminar Vortex Technology: A Review. *Micromachines* **2019**, *10*, 594. [CrossRef]
7. Gossett, D.R.; Weaver, W.M.; Mach, A.J.; Hur, S.C.; Tse, H.T.K.; Lee, W.; Amini, H.; Di Carlo, D. Label-free cell separation and sorting in microfluidic systems. *Anal. Bioanal. Chem.* **2010**, *397*, 3249–3267. [CrossRef] [PubMed]
8. Zhang, J.; Yan, S.; Sluyter, R.; Li, W.; Alici, G.; Nguyen, N.T. Inertial particle separation by differential equilibrium positions in a symmetrical serpentine micro-channel. *Sci. Rep.* **2014**, *4*, 4527. [CrossRef] [PubMed]
9. Yamada, M.; Nakashima, M.; Seki, M. Pinched flow fractionation: Continuous size separation of particles utilizing a laminar flow profile in a pinched microchannel. *Anal. Chem.* **2004**, *76*, 5465–5471. [CrossRef] [PubMed]
10. Blahout, S.; Reinecke, S.R.; Tabaei Kazerooni, H.; Kruggel-Emden, H.; Hussong, J. On the 3D distribution and size fractionation of microparticles in a serpentine microchannel. *Microfluid. Nanofluid.* **2020**, *24*, 22. [CrossRef]
11. McGrath, J.; Jimenez, M.; Bridle, H. Deterministic lateral displacement for particle separation: A review. *Lab Chip* **2014**, *14*, 4139–4158. [CrossRef] [PubMed]
12. Crowley, T.A.; Pizziconi, V. Isolation of plasma from whole blood using planar microfilters for lab-on-a-chip applications. *Lab Chip* **2005**, *5*, 922–929. [CrossRef] [PubMed]
13. Bayareh, M. An updated review on particle separation in passive microfluidic devices. *Chem. Eng. Process.-Process Intensif.* **2020**, *153*, 107984. [CrossRef]
14. Xuan, X. Recent advances in direct current electrokinetic manipulation of particles for microfluidic applications. *Electrophoresis* **2019**, *40*, 2484–2513. [CrossRef]
15. Lösch, P.; Nikolaus, K.; Antonyuk, S. Fractionating of finest particles using cross-flow separation with superimposed electric field. *Sep. Purif. Technol.* **2021**, *257*, 117820. [CrossRef]
16. Giesler, J.; Weirauch, L.; Thöming, J.; Baune, M.; Pesch, G.R. Separating microparticles by material and size using dielectrophoretic chromatography with frequency modulation. *Sci. Rep.* **2021**, *11*, 16861. [CrossRef] [PubMed]
17. Kelland, D.R. Magnetic separation of nanoparticles. *IEEE Trans. Magn.* **1998**, *34*, 2123–2125. [CrossRef]
18. Xuan, X. Recent Advances in Continuous-Flow Particle Manipulations Using Magnetic Fluids. *Micromachines* **2019**, *10*, 744. [CrossRef]
19. Rhein, F.; Zhai, O.; Schmid, E.; Nirschl, H. Multidimensional Separation by Magnetic Seeded Filtration: Experimental Studies. *Powders* **2023**, *2*, 588–606. [CrossRef]
20. Destgeer, G.; Sung, H.J. Recent advances in microfluidic actuation and micro-object manipulation via surface acoustic waves. *Lab Chip* **2015**, *15*, 2722–2738. [CrossRef]
21. Wu, M.; Ozcelik, A.; Rufo, J.; Wang, Z.; Fang, R.; Jun Huang, T. Acoustofluidic separation of cells and particles. *Microsyst. Nanoeng.* **2019**, *5*, 32. [CrossRef] [PubMed]

22. Wiklund, M. Acoustofluidics 12: Biocompatibility and cell viability in microfluidic acoustic resonators. *Lab Chip* **2012**, *12*, 2018–2028. [CrossRef]
23. Ding, X.; Li, P.; Lin, S.C.S.; Stratton, Z.S.; Nama, N.; Guo, F.; Slotcavage, D.; Mao, X.; Shi, J.; Costanzo, F.; et al. Surface acoustic wave microfluidics. *Lab Chip* **2013**, *13*, 3626–3649. [CrossRef]
24. Gao, Y.; Wu, M.; Lin, Y.; Xu, J. Acoustic Microfluidic Separation Techniques and Bioapplications: A Review. *Micromachines* **2020**, *11*, 921. [CrossRef] [PubMed]
25. Fan, Y.; Wang, X.; Ren, J.; Lin, F.; Wu, J. Recent advances in acoustofluidic separation technology in biology. *Microsyst. Nanoeng.* **2022**, *8*, 94. [CrossRef] [PubMed]
26. Collins, D.J.; Neild, A.; Ai, Y. Highly focused high-frequency travelling surface acoustic waves (SAW) for rapid single-particle sorting. *Lab Chip* **2016**, *16*, 471–479. [CrossRef] [PubMed]
27. Behrens, J.; Langelier, S.; Rezk, A.R.; Lindner, G.; Yeo, L.Y.; Friend, J.R. Microscale anechoic architecture: Acoustic diffusers for ultra low power microparticle separation via traveling surface acoustic waves. *Lab Chip* **2015**, *15*, 43–46. [CrossRef] [PubMed]
28. Shi, J.; Ahmed, D.; Mao, X.; Lin, S.C.S.; Lawit, A.; Huang, T.J. Acoustic tweezers: Patterning cells and microparticles using standing surface acoustic waves (SSAW). *Lab Chip* **2009**, *9*, 2890–2895. [CrossRef] [PubMed]
29. Liu, G.; He, F.; Li, X.; Zhao, H.; Zhang, Y.; Li, Z.; Yang, Z. Multi-level separation of particles using acoustic radiation force and hydraulic force in a microfluidic chip. *Microfluid. Nanofluid.* **2019**, *23*, 23. [CrossRef]
30. Jo, M.C.; Guldiken, R. Active density-based separation using standing surface acoustic waves. *Sensors Actuators A Phys.* **2012**, *187*, 22–28. [CrossRef]
31. Gupta, S.; Feke, D.L.; Manas-Zloczower, I. Fractionation of mixed particulate solids according to compressibility using ultrasonic standing wave fields. *Chem. Eng. Sci.* **1995**, *50*, 3275–3284. [CrossRef]
32. Li, P.; Zhong, J.; Liu, N.; Lu, X.; Liang, M.; Ai, Y. Physical properties-based microparticle sorting at submicron resolution using a tunable acoustofluidic device. *Sensors Actuators B Chem.* **2021**, *344*, 130203. [CrossRef]
33. Laurell, T.; Petersson, F.; Nilsson, A. Chip integrated strategies for acoustic separation and manipulation of cells and particles. *Chem. Soc. Rev.* **2007**, *36*, 492–506. [CrossRef] [PubMed]
34. Zhao, S.; Wu, M.; Yang, S.; Wu, Y.; Gu, Y.; Chen, C.; Ye, J.; Xie, Z.; Tian, Z.; Bachman, H.; et al. A disposable acoustofluidic chip for nano/microparticle separation using unidirectional acoustic transducers. *Lab Chip* **2020**, *20*, 1298–1308. [CrossRef]
35. Wu, M.; Huang, P.H.; Zhang, R.; Mao, Z.; Chen, C.; Kemeny, G.; Li, P.; Lee, A.V.; Gyanchandani, R.; Armstrong, A.J.; et al. Circulating Tumor Cell Phenotyping via High-Throughput Acoustic Separation. *Small* **2018**, *14*, e1801131. [CrossRef] [PubMed]
36. Ding, X.; Peng, Z.; Lin, S.C.S.; Geri, M.; Li, S.; Li, P.; Chen, Y.; Dao, M.; Suresh, S.; Huang, T.J. Cell separation using tilted-angle standing surface acoustic waves. *Proc. Natl. Acad. Sci. USA* **2014**, *111*, 12992–12997. [CrossRef] [PubMed]
37. Sehgal, P.; Kirby, B.J. Separation of 300 and 100 nm Particles in Fabry-Perot Acoustofluidic Resonators. *Anal. Chem.* **2017**, *89*, 12192–12200. [CrossRef]
38. Cheeke, J.D.N. *Fundamentals and Applications of Ultrasonic Waves*; CRC series in pure and applied physics; CRC Press: Boca Raton, FL, USA, 2002.
39. Yeo, L.Y.; Friend, J.R. Surface Acoustic Wave Microfluidics. *Annu. Rev. Fluid Mech.* **2014**, *46*, 379–406. [CrossRef]
40. Devendran, C.; Albrecht, T.; Brenker, J.; Alan, T.; Neild, A. The importance of travelling wave components in standing surface acoustic wave (SSAW) systems. *Lab Chip* **2016**, *16*, 3756–3766. [CrossRef] [PubMed]
41. Nyborg, W.L. Acoustic Streaming due to Attenuated Plane Waves. *J. Acoust. Soc. Am.* **1953**, *25*, 68–75. [CrossRef]
42. Settnes, M.; Bruus, H. Forces acting on a small particle in an acoustical field in a viscous fluid. *Phys. Rev. E Stat. Nonlinear Soft Matter Phys.* **2012**, *85*, 016327. [CrossRef] [PubMed]
43. Kondoh, J.; Shimizu, N.; Matsui, Y.; Shiokawa, S. Liquid heating effects by SAW streaming on the piezoelectric substrate. *IEEE Trans. Ultrason. Ferroelectr. Freq. Control* **2005**, *52*, 1881–1883. [CrossRef]
44. Shilton, R.J.; Mattoli, V.; Travagliati, M.; Agostini, M.; Desii, A.; Beltram, F.; Cecchini, M. Rapid and Controllable Digital Microfluidic Heating by Surface Acoustic Waves. *Adv. Funct. Mater.* **2015**, *25*, 5895–5901. [CrossRef]
45. Das, P.K.; Snider, A.D.; Bhethanabotla, V.R. Acoustothermal heating in surface acoustic wave driven microchannel flow. *Phys. Fluids* **2019**, *31*, 106106. [CrossRef]
46. Sachs, S.; Fröhlich, T.; Schumacher, J. Suppression of free convection effects for spherical 1 kg mass prototype. *Int. J. Heat Mass Transf.* **2021**, *170*, 121037. [CrossRef]
47. Koklu, M.; Sabuncu, A.C.; Beskok, A. Acoustophoresis in shallow microchannels. *J. Colloid Interface Sci.* **2010**, *351*, 407–414. [CrossRef] [PubMed]
48. Peng, T.; Zhou, M.; Yuan, S.; Fan, C.; Jiang, B. Numerical investigation of particle deflection in tilted-angle standing surface acoustic wave microfluidic devices. *Appl. Math. Model.* **2022**, *101*, 517–532. [CrossRef]
49. Kiebert, F.; Wege, S.; Massing, J.; König, J.; Cierpka, C.; Weser, R.; Schmidt, H. 3D measurement and simulation of surface acoustic wave driven fluid motion: A comparison. *Lab Chip* **2017**, *17*, 2104–2114. [CrossRef] [PubMed]

50. König, J.; Chen, M.; Rösing, W.; Boho, D.; Mäder, P.; Cierpka, C. On the use of a cascaded convolutional neural network for three-dimensional flow measurements using astigmatic PTV. *Meas. Sci. Technol.* **2020**, *31*, 074015. [CrossRef]
51. Sachs, S.; Baloochi, M.; Cierpka, C.; König, J. On the acoustically induced fluid flow in particle separation systems employing standing surface acoustic waves-Part I. *Lab Chip* **2022**, *22*, 2011–2027. [CrossRef]
52. Cierpka, C.; Segura, R.; Hain, R.; Kähler, C.J. A simple single camera 3C3D velocity measurement technique without errors due to depth of correlation and spatial averaging for microfluidics. *Meas. Sci. Technol.* **2010**, *21*, 045401. [CrossRef]
53. Cierpka, C.; Rossi, M.; Segura, R.; Kähler, C.J. On the calibration of astigmatism particle tracking velocimetry for microflows. *Meas. Sci. Technol.* **2011**, *22*, 015401. [CrossRef]
54. Sachs, S.; Cierpka, C.; König, J. On the acoustically induced fluid flow in particle separation systems employing standing surface acoustic waves-Part II. *Lab Chip* **2022**, *22*, 2028–2040. [CrossRef] [PubMed]
55. Sachs, S.; Ratz, M.; Mäder, P.; König, J.; Cierpka, C. Particle detection and size recognition based on defocused particle images: A comparison of a deterministic algorithm and a deep neural network. *Exp. Fluids* **2023**, *64*, 21. [CrossRef]
56. Ratz, M.; Sachs, S.; König, J.; Cierpka, C. A deep neural network architecture for reliable 3D position and size determination for Lagrangian particle tracking using a single camera. *Meas. Sci. Technol.* **2023**, *34*, 105203. [CrossRef]
57. Sachs, S.; Schmidt, H.; Cierpka, C.; König, J. On the behavior of prolate spheroids in a standing surface acoustic wave field. *Microfluid. Nanofluid.* **2023**, *27*, 81. [CrossRef]
58. Sachs, S.; Schreier, D.; Brand, F.; Drese, K.S.; Cierpka, C.; König, J. Interplay of acoustophoresis and dielectrophoresis in a standing surface acoustic wave field: From spherical to non-spherical particles. *Microfluid. Nanofluid.* **2024**, *28*, 67. [CrossRef]
59. Bruus, H. Acoustofluidics 2: Perturbation theory and ultrasound resonance modes. *Lab Chip* **2012**, *12*, 20–28. [CrossRef] [PubMed]
60. Barnkob, R.; Nama, N.; Ren, L.; Huang, T.J.; Costanzo, F.; Kähler, C.J. Acoustically Driven Fluid and Particle Motion in Confined and Leaky Systems. *Phys. Rev. Appl.* **2018**, *9*, 014027. [CrossRef]
61. Muller, P.B.; Barnkob, R.; Jensen, M.J.H.; Bruus, H. A numerical study of microparticle acoustophoresis driven by acoustic radiation forces and streaming-induced drag forces. *Lab Chip* **2012**, *12*, 4617–4627. [CrossRef] [PubMed]
62. Landau, L.D.; Lifshitz, E.M. *Fluid Mechanics*, 2nd ed.; Pergamon Press: Oxford, UK, 1987.
63. COMSOL AB. COMSOL Multiphysics. Available online: https://www.comsol.com/ (accessed on 15 April 2021).
64. Joergensen, J.H.; Bruus, H. Theory of pressure acoustics with thermoviscous boundary layers and streaming in elastic cavities. *J. Acoust. Soc. Am.* **2021**, *149*, 3599. [CrossRef]
65. Joergensen, J.H. Theory and Modeling of Thermoviscous Acoustofluidics. Ph.D. Thesis, Technical University of Denmark, Lyngby, Denmark, 2022.
66. Doinikov, A.A. Acoustic radiation force on a spherical particle in a viscous heat-conducting fluid. I. General formula. *J. Acoust. Soc. Am.* **1997**, *101*, 713–721. [CrossRef]
67. Karlsen, J.T.; Qiu, W.; Augustsson, P.; Bruus, H. Acoustic Streaming and Its Suppression in Inhomogeneous Fluids. *Phys. Rev. Lett.* **2018**, *120*, 054501. [CrossRef] [PubMed]
68. Dual, J.; Hahn, P.; Leibacher, I.; Möller, D.; Schwarz, T.; Wang, J. Acoustofluidics 19: Ultrasonic microrobotics in cavities: Devices and numerical simulation. *Lab Chip* **2012**, *12*, 4010–4021. [CrossRef] [PubMed]
69. Arzt, R.M.; Salzmann, E.; Dransfeld, K. Elastic Surface Waves in Quartz at 316 MHz. *Appl. Phys. Lett.* **1967**, *10*, 165–167. [CrossRef]
70. Dentry, M.B.; Friend, J.R.; Yeo, L.Y. Continuous flow actuation between external reservoirs in small-scale devices driven by surface acoustic waves. *Lab Chip* **2014**, *14*, 750–758. [CrossRef] [PubMed]
71. Winkler, A. SAW-Basierte, Modulare Mikrofluidiksysteme Hoher Flexibilität. Ph.D. Thesis, Technische Universität Dresden, Dresden, Germany, 2011.
72. Bruus, H. *Theoretical Microfluidics*; Oxford University Press: Oxford, UK, 2007.
73. Schach, E.; Buchmann, M.; Tolosana-Delgado, R.; Leißner, T.; Kern, M.; van den Gerald Boogaart, K.; Rudolph, M.; Peuker, U.A. Multidimensional characterization of separation processes–Part 1: Introducing kernel methods and entropy in the context of mineral processing using SEM-based image analysis. *Miner. Eng.* **2019**, *137*, 78–86. [CrossRef]
74. Buchmann, M.; Schach, E.; Leißner, T.; Kern, M.; Mütze, T.; Rudolph, M.; Peuker, U.A.; Tolosana-Delgado, R. Multidimensional characterization of separation processes–Part 2: Comparability of separation efficiency. *Miner. Eng.* **2020**, *150*, 106284. [CrossRef]
75. Wilhelm, T.; Sygusch, J.; Furat, O.; Bachmann, K.; Rudolph, M.; Schmidt, V. Parametric Stochastic Modeling of Particle Descriptor Vectors for Studying the Influence of Ultrafine Particle Wettability and Morphology on Flotation-Based Separation Behavior. *Powders* **2023**, *2*, 353–371. [CrossRef]
76. Lee, S.H.; Cha, B.; Yi, H.G.; Kim, J.; Jeon, J.S.; Park, J. Acoustofluidic separation of bacteria from platelets using tilted-angle standing surface acoustic wave. *Sensors Actuators B Chem.* **2024**, *417*, 136161. [CrossRef]
77. Fakhfouri, A.; Devendran, C.; Albrecht, T.; Collins, D.J.; Winkler, A.; Schmidt, H.; Neild, A. Surface acoustic wave diffraction driven mechanisms in microfluidic systems. *Lab Chip* **2018**, *18*, 2214–2224. [CrossRef]

78. Weser, R.; Winkler, A.; Weihnacht, M.; Menzel, S.; Schmidt, H. The complexity of surface acoustic wave fields used for microfluidic applications. *Ultrasonics* **2020**, *106*, 106160. [CrossRef]
79. Devendran, C.; Collins, D.J.; Neild, A. The role of channel height and actuation method on particle manipulation in surface acoustic wave (SAW)-driven microfluidic devices. *Microfluid. Nanofluid.* **2022**, *26*, 9. [CrossRef]
80. Collins, D.J.; O'Rorke, R.; Devendran, C.; Ma, Z.; Han, J.; Neild, A.; Ai, Y. Self-Aligned Acoustofluidic Particle Focusing and Patterning in Microfluidic Channels from Channel-Based Acoustic Waveguides. *Phys. Rev. Lett.* **2018**, *120*, 074502. [CrossRef]
81. Sachs, S.; Schreier, D.; König, J.; Cierpka, C. *On the Fabrication of a SAW-Based Mircofluidic Device with Raised Acoustic Energy Density and Tailored Acoustic Pressure Field Using Dry Film Resist*; Acoustofluidics: Uppsala, Sweden, 2024.
82. Lenshof, A.; Evander, M.; Laurell, T.; Nilsson, J. Acoustofluidics 5: Building microfluidic acoustic resonators. *Lab Chip* **2012**, *12*, 684–695. [CrossRef] [PubMed]
83. Wijaya, F.B.; Lim, K.M. Numerical Calculation of Acoustic Radiation Force and Torque Acting on Rigid Non-spherical Particles. *Acta Acust. United Acust.* **2015**, *101*, 531–542. [CrossRef]
84. Khan, M.S.; Ali, M.; Lee, S.H.; Jang, K.Y.; Lee, S.J.; Park, J. Acoustofluidic separation of prolate and spherical micro-objects. *Microsystems Nanoeng.* **2024**, *10*, 6. [CrossRef]
85. Weirauch, L.; Giesler, J.; Baune, M.; Pesch, G.R.; Thöming, J. Shape-selective remobilization of microparticles in a mesh-based DEP filter at high throughput. *Sep. Purif. Technol.* **2022**, *300*, 121792. [CrossRef]
86. Tohme, T.; Magaud, P.; Baldas, L. Transport of Non-Spherical Particles in Square Microchannel Flows: A Review. *Micromachines* **2021**, *12*, 277. [CrossRef]
87. Lauricella, G.; Zhou, J.; Luan, Q.; Papautsky, I.; Peng, Z. Computational study of inertial migration of prolate particles in a straight rectangular channel. *Phys. Fluids* **2022**, *34*, 082021. [CrossRef]
88. Tai, C.W.; Wang, S.; Narsimhan, V. Cross–stream migration of nonspherical particles in second–order fluid flows: Effect of flow profiles. *AIChE J.* **2020**, *66*, e17076. [CrossRef]
89. Tai, C.W.; Narsimhan, V. Experimental and theoretical studies of cross-stream migration of non-spherical particles in a quadratic flow of a viscoelastic fluid. *Soft Matter* **2022**, *18*, 4613–4624. [CrossRef]
90. de Timary, G.; Rousseau, C.J.; van Melderen, L.; Scheid, B. Shear-enhanced sorting of ovoid and filamentous bacterial cells using pinch flow fractionation. *Lab Chip* **2022**, *23*, 659–670. [CrossRef] [PubMed]
91. Schwarz, T.; Petit-Pierre, G.; Dual, J. Rotation of non-spherical micro-particles by amplitude modulation of superimposed orthogonal ultrasonic modes. *J. Acoust. Soc. Am.* **2013**, *133*, 1260–1268. [CrossRef]
92. Schwarz, T.; Hahn, P.; Petit-Pierre, G.; Dual, J. Rotation of fibers and other non-spherical particles by the acoustic radiation torque. *Microfluid. Nanofluid.* **2015**, *18*, 65–79. [CrossRef]
93. Hahn, P.; Leibacher, I.; Baasch, T.; Dual, J. Numerical simulation of acoustofluidic manipulation by radiation forces and acoustic streaming for complex particles. *Lab Chip* **2015**, *15*, 4302–4313. [CrossRef]
94. Garbin, A.; Leibacher, I.; Hahn, P.; Le Ferrand, H.; Studart, A.; Dual, J. Acoustophoresis of disk-shaped microparticles: A numerical and experimental study of acoustic radiation forces and torques. *J. Acoust. Soc. Am.* **2015**, *138*, 2759–2769. [CrossRef] [PubMed]
95. Leão-Neto, J.P.; Lopes, J.H.; Silva, G.T. Acoustic radiation torque exerted on a subwavelength spheroidal particle by a traveling and standing plane wave. *J. Acoust. Soc. Am.* **2020**, *147*, 2177. [CrossRef] [PubMed]
96. Lima, E.B.; Leão-Neto, J.P.; Marques, A.S.; Silva, G.C.; Lopes, J.H.; Silva, G.T. Nonlinear Interaction of Acoustic Waves with a Spheroidal Particle: Radiation Force and Torque Effects. *Phys. Rev. Appl.* **2020**, *13*, 064048. [CrossRef]
97. Zareei, S.M.; Sepehrirahnama, S.; Jamshidian, M.; Ziaei-Rad, S. Three-dimensional numerical simulation of particle acoustophoresis: COMSOL implementation and case studies. *Eng. Comput.* **2023**, *39*, 735–750. [CrossRef]
98. Fakhfouri, A.; Colditz, M.; Devendran, C.; Ivanova, K.; Jacob, S.; Neild, A.; Winkler, A. Fully Microfabricated Surface Acoustic Wave Tweezer for Collection of Submicron Particles and Human Blood Cells. *ACS Appl. Mater. Interfaces* **2023**, *15*, 24023–24033. [CrossRef] [PubMed]
99. Ley, M.W.H.; Bruus, H. Three-Dimensional Numerical Modeling of Acoustic Trapping in Glass Capillaries. *Phys. Rev. Appl.* **2017**, *8*, 024020. [CrossRef]
100. Skov, N.R.; Bruus, H. Modeling of Microdevices for SAW-Based Acoustophoresis—A Study of Boundary Conditions. *Micromachines* **2016**, *7*, 182. [CrossRef] [PubMed]


**Disclaimer/Publisher's Note:** The statements, opinions and data contained in all publications are solely those of the individual author(s) and contributor(s) and not of MDPI and/or the editor(s). MDPI and/or the editor(s) disclaim responsibility for any injury to people or property resulting from any ideas, methods, instructions or products referred to in the content.